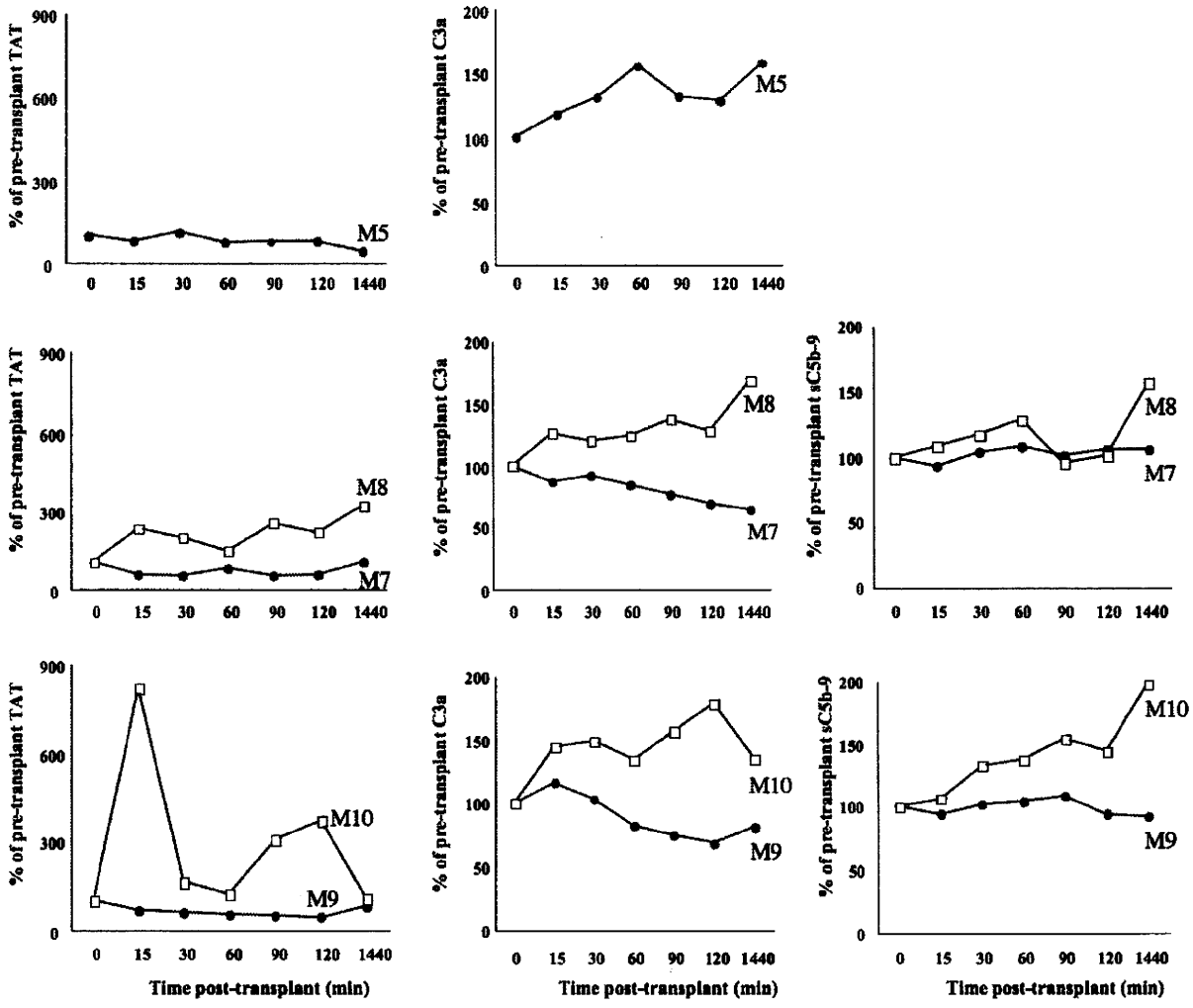

Fig. 2. EDTA blood was drawn from a femoral vein catheter of the transplanted monkeys treated with heparin (squares) or LMW-DS (circles) at varying time points after porcine islet xenotransplantation. TAT, C3a, and sC5b--9 levels were assessed and expressed as percentage of the pre-transplant values.

Immunohistochemical staining of grafted pig islets after intraportal transplantation into monkeys treated with LMW-DS or heparin

The immunohistochemical findings from the grafts were summarized in Fig. 4 and Table 2. As expected, most parameters involved in innate immune responses were active after 24 h post-islet transplantation in the controls M8 and M10. In particular, CD68+ macrophages, and neutrophil elastase positive PMNs were abrogated in the monkeys treated with LMW-DS compared with the controls given heparin. Also, CD41+ platelets tended to be lower in the LMW-DS treated animals. CD56+ natural killer cells were found only occasionally. Unlike the soluble complement markers there was no clear inhibition of complement activation as reflected in deposition of C3 fragments and C9 on the surface of the islets. Furthermore, IgM antibodies were found on islet both in LMW-DS and heparin-treated animals. Most of parameters reflecting specific immune responses were yet silent. However, CD3+ T-cell infiltration was already seen in the islet grafts of the controls M8 and M10. Notably, this infiltration was effectively suppressed by LMW-DS.

Binding of complement components to porcine islets after incubation in human plasma

After incubation in hirudin-treated plasma, the porcine islets were stained with FITC-conjugated antibodies recognizing IgG, IgM, C1q, C3b/iC3b, C4 fragments, C9, and MBL. Large particle flow cytometry and confocal microscopy demonstrated that antibodies against IgG, IgM, C1q, C4, and C3

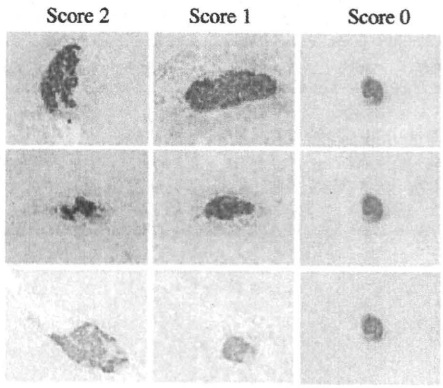

Fig. 3. Visual examples of the morphological scoring system used to quantify different aspects of the IBMIR. Hematoxylin eosin-stained porcine islet grafts retrieved 24 h after intraportal xenotransplantation from diabetic monkeys treated with LMW-DS or heparin were used. A summary of all transplanted monkeys is presented in Table 1.

bound strongly to the islets, but the binding of MBL and C9 was less prominent (Fig. 5A and B). C3b/iC3b fragments were detected on the islets after only 5 min, and the binding of C3b/iC3b continued to increase over time. Addition of Compstatin significantly reduced the binding of C3b/iC3b to the islets (Fig. 5C). Confocal microscopy analyses confirmed these results (not shown).

Inhibition of complement activation by LMW-DS and Compstatin

Ten percentage (v/v) human serum was incubated in wells of microtiter plates in the presence of LMW-DS and/or Compstatin for 30 min at 37 °C (Fig. 6). In the presence of Compstatin there was no effect below 0.5 μM of the compound, but at higher concentrations Compstatin gradually inhibited complement activation. At 5 μM total inhibition was achieved. LMW-DS inhibited complement activation only marginally between 10 and 100 mg/l, but the effect was more pronounced at concentrations above this level. There was no indication of interaction between the drugs regarding this effect on complement activation in serum.

Discussion

We have previously shown that LMW-DS efficiently prevents clotting that occurs in both allogeneic and xenogeneic IBMIR triggered by APIs both in vitro and in vivo in a small animal model [9,18]. Here, we confirm that LMW-DS is efficient also in a primate model mimicking the clinical setting. The effect of LMW-DS was compared with that of heparin, which is routinely used in clinical islet transplantation. LMW-DS was proved to be

Table 1. Summary of the morphological score (as depicted in Fig. 3) of the islets grafts in recipient monkeys M5 and M7–M10

Monkey number	Treatment	Integrity	Thrombus	Cell infiltration	Percentage of score 0[a] (%)	APTT at 24 h after transplantation (s)
M5	LMW-DS, n = 113	0.66 ± 0.04[b]	0.26 ± 0.03	0.90 ± 0.07	37.2	101
M7	LMW-DS, n = 134	0.93 ± 0.06	0.52 ± 0.06	1.08 ± 0.06	26.1	66
M8	Heparin, n = 149	1.05 ± 0.05	0.62 ± 0.06	1.17 ± 0.06	20.1	24
P-value[c]		0.13	0.28	0.32	0.23	
M9	LMW-DS, n = 134	0.63 ± 0.05	0.37 ± 0.05	0.85 ± 0.06	44.0	107
M10	Heparin, n = 125	0.95 ± 0.06	0.54 ± 0.06	1.25 ± 0.07	22.4	25
P-value[d]		<0.0001	<0.05	<0.0001	<0.001	

[a]Percentage islets with no signs of IBMIR (score 0); [b]Values are expressed as mean ± SEM; [c]P-values for M7 and M8; [d]P-values for M9 and M10. APTT, activated partial thromboplastin time; IBMIR, instant blood-mediated inflammatory reaction; LMW-DS, Low molecular weight dextran sulfate.

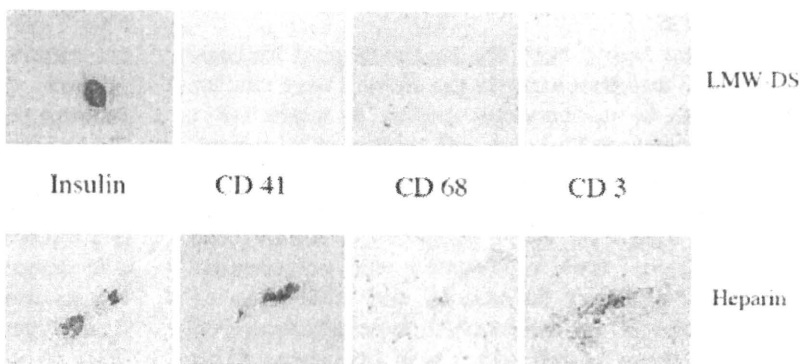

Fig. 4. Immunohistochemical staining of porcine islet grafts retrieved 24 h after intraportal xenotransplantation from diabetic monkeys treated with LMW-DS or heparin. The figure shows representative expression of insulin and of CD41 (platelets), CD68 (macrophages), and CD3 (T cells) in the grafts. A summary of all transplanted monkeys is presented in Table 2. Magnification 200×.

Table 2. Summary of the immunohistochemical staining (as depicted in Fig. 4) of the islet grafts in recipient monkeys receiving LMW-DS or heparin

Treatment	CD41	C3c	C9	Neutrophil elastase	CD68	MAC 387	CD56	CD3	CD20	IgG	IgM
LMW-DS	(−)-(++)	(−)-(++)	(−)-(+++)	(−)-(++)	(−)-(++)	(−)-(++)	(−)-(+)	(−)-(++)	(−)-(+)	(−)	(−)-(+)
(n = 21)	0.59 ± 0.19[a]	0.80 ± 0.37	1.50 ± 0.31	0.42 ± 0.23	1.31 ± 0.21	0.90 ± 0.28	0.10 ± 0.10	0.63 ± 0.20	0.20 ± 0.13	0	0.25 ± 0.25
Heparin (n = 18)	(−)-(+++)	(−)-(++)	(−)-(+++)	(−)-(++)	(++)-(+++)	(+)-(+++)	(−)-(+)	(−)-(+++)	(−)-(++)	(−)	(−)-(++)
	1.60 ± 0.51	0.63 ± 0.26	1.67 ± 0.33	1.08 ± 0.23	2.17 ± 0.11	2.11 ± 0.26	0.22 ± 0.15	1.90 ± 0.35	0.40 ± 0.27	0	0.60 ± 0.24
P value	0.056	0.69	0.71	0.04	0.002	0.01	0.48	0.006	0.83	–	0.36

[a]Values are expressed as mean ± SEM. LMW-DS, Low molecular weight dextran sulfate.

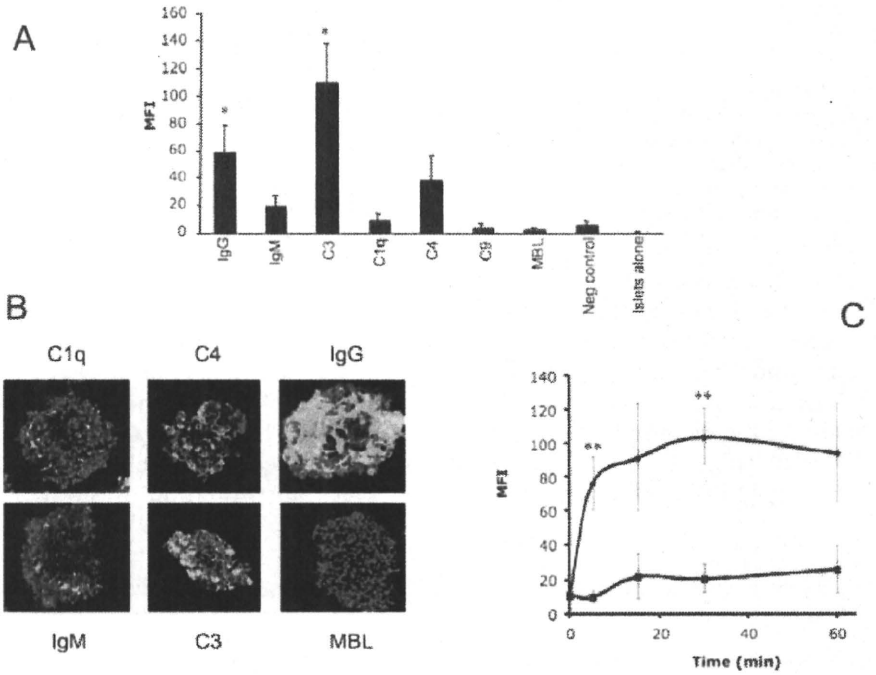

Fig. 5. Porcine islets incubated in hirudin-treated plasma for 30 min. The islets were stained for IgG (n = 5), IgM (n = 5), C3b/iC3b (n = 5), C1q (n = 3), C4 (n = 5), C9 (n = 3), and MBL (n = 3). As negative control, an antibody recognizing mouse IgG was used (n = 5). The islets were analyzed by (A) large particle flow cytometry and (B) confocal microscopy. In (C), the deposition of C3b/iC3b on the islet in the absence and presence of Compstatin is presented after analysis by large particle flow cytometry (n = 5; statistical evaluation was performed at 5 and 30 min where n = 7; *P < 0.05 and **P < 0.01).

far more efficient in inhibiting the IBMIR than heparin. These data confirm those of Rood et al. [19] who recently demonstrated longer porcine islet survival in non-human primates treated with LMW-DS.

In this study, both the morphological findings and the measurements in the plasma were similar to those in our previous studies, in which APIs were surrounded by clots and infiltrated by numerous leukocytes immediately after contact with fresh blood seen in the tubing loop model and our small animal model [9]. Most parameters reflecting the IBMIR, i.e. both coagulation and complement cascades, platelet deposition, and infiltration of macrophages and neutrophils, were attenuated in the monkeys treated with LMW-DS compared to the controls. There was also a tendency that increases in granulocyte count and liver enzymes were attenuated. One control monkey (M6) died of hypoglycemia, suggesting a strong IBMIR. Notably, T-cell infiltration observed in some of the transplanted islet grafts was also effectively suppressed, demonstrating that also the adaptive immune responses are attenuated by LMW-DS.

The effects of LMW-DS on the adaptive immune system may be explained by the effects on complement activation as complement is also of great importance in bridging innate immunity and specific immune responses. In allogeneic whole organ transplantation, C3 is one of the essential factors that trigger rejection in mice [20–22] and humans [23]. It is therefore reasonable to expect that

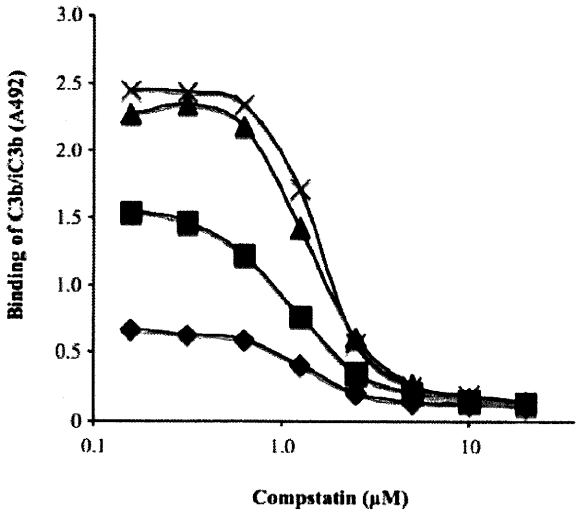

Fig. 6. Binding of C3b/iC3b to the surface of microtiter wells after incubation with 10% serum in the presence of increasing doses of Compstatin for 30 min at 37 °C. 0 (cross), 10 (triangle), 100 (squares), and 1000 (diamond) mg/l of LMW-DS was present in the wells.

complement activation will trigger a profound adaptive immune response raised against the graft, necessitating an unwarrantedly heavy immunosuppressive regimen. Previous studies support such a hypothesis [4,5].

As shown in Table 1, the islet grafts in M9 that reached an APTT of 107 s 24 h after transplantation, demonstrated well-preserved morphology suggesting that this dose of LMW-DS would be preferable. In a recently performed phase I study in normal individuals, we have shown that this concentration can be reached without an increased risk of bleeding or side effects (manuscript under preparation). This makes treatment with LMW-DS during xenogeneic islet transplantation an attractive alternative. It should be noted that a specific concentration of LMW-DS gives different APTT in blood from different individuals both in vitro and in vivo, probably due to that different allotypes of certain coagulation factors interact with LMW-DS differently.

In our previous studies, we showed that complement activation induced in xenogeneic IBMIR occurs secondarily to coagulation activation; a reaction which is also seen in allogeneic IBMIR [9,24] and which is elicited by chondroitin sulfate released by activated platelets [25]. This explains why complement activation in this study was suppressed in parallel with the reduction of coagulation activation at substantially lower concentrations (15–35 mg/l) of LMW-DS than used in other studies aiming for a inhibition of hyper acute rejection [26,27]. However, unlike complement activation in the fluid phase, immunohistochemical analyses showed that complement deposition was still seen on the islet grafts in the monkeys treated with LMW-DS. These reactions were analyzed in detail in vitro using large particle flow cytometry and confocal microscopy to be able to clarify the mechanism of activation. The experiments were performed using human plasma to directly translate the findings to clinical islet xenotransplantation. Pig islets incubated in human plasma revealed an almost instantaneous binding of IgM and IgG antibodies and complement components already after 5 min. This rapid activation was completely inhibited by Compstatin. It is possible that the instantaneous insulin dumping in a non-human primate model previously reported by Bennet et al. [3] and also observed in monkey M6 is explained by this antibody-mediated reaction. The severity of this reaction, which was totally abrogated by the recombinant complement inhibitor CR1, is reflected in the fact that the release of insulin corresponded to about 40% of the insulin in the transplanted islets.

One way to fully inhibit complement activation is to increase the dose of LMW-DS, but as shown in our in vitro experiments, doses between 10 and 100 mg/l have only minor effects on complement activation alone. Moreover, higher doses of LMW-DS are likely to give side effects. It is therefore obvious that LMW-DS must be combined with a specific complement inhibitor such as Compstatin to block the immediate destructive immunoglobulin-triggered complement activation found both in vitro and in vivo [10,28]. The in vitro studies show that LMW-DS and Compstatin do not interact in human serum.

Taken together, it possible to propose a model of how the different components of IBMIR interact in xenogeneic combinations: (1) Immediately when porcine islets come in contact with human blood there is an instantaneous binding of IgG and IgM antibodies to the islet surface which triggers a deleterious complement activation; (2) This is followed by a clotting reaction with accompanying complement activation. Based upon the experimental data presented, LMW-DS combined with a specific complement inhibitor is an attractive alternative to control the detrimental innate immune responses that are postulated to occur in forthcoming intraportal pre-clinical and clinical islet xenotransplantation trials. We are at the moment in progress to produce sufficient amounts of Compstatin to perform studies in the NHP model with Compstatin combined with LMW-DS.

Acknowledgments

This work was supported by National Institute of Health Grants 5U01-A1065192, GM-62134, GM069736, and AI068730, Juvenile Diabetes Research Foundation, 1-2004-18, Swedish Research Council Grants 5647, and 15244.

References

1. SHAPIRO AM, LAKEY JR, RYAN EA et al. Islet transplantation in seven patients with type 1 diabetes mellitus using a glucocorticoid-free immunosuppressive regimen. N Engl J Med 2000; 343: 230.
2. ROOD PP, BUHLER LH, BOTTINO R, TRUCCO M, COOPER DK. Pig-to-nonhuman primate islet xenotransplantation: a review of current problems. Cell Transplant 2006; 15: 89.
3. BENNET W, SUNDBERG B, LUNDGREN T et al. Damage to porcine islets of Langerhans after exposure to human blood *in vitro*, or after intraportal transplantation to cynomologus monkeys: protective effects of sCR1 and heparin. Transplantation 2000; 69: 711.
4. BUHLER L, DENG S, O'NEIL J et al. Adult porcine islet transplantation in baboons treated with conventional immunosuppression or a non-myeloablative regimen and CD154 blockade. Xenotransplantation 2002; 9: 3.
5. CANTAROVICH D, BLANCHO G, POTIRON N et al. Rapid failure of pig islet transplantation in non human primates. Xenotransplantation 2002; 9: 25.
6. KIRCHHOF N, SHIBATA S, WIJKSTROM M et al. Reversal of diabetes in non-immunosuppressed rhesus macaques by intraportal porcine islet xenografts precedes acute cellular rejection. Xenotransplantation 2004; 11: 396.
7. CARDONA K, KORBUTT GS, MILAS Z et al. Long-term survival of neonatal porcine islets in nonhuman primates by targeting costimulation pathways. Nat Med 2006; 12: 304.
8. HERING BJ, WIJKSTROM M, GRAHAM ML et al. Prolonged diabetes reversal after intraportal xenotransplantation of wild-type porcine islets in immunosuppressed nonhuman primates. Nat Med 2006; 12: 301.
9. GOTO M, JOHANSSON H, MAEDA A, ELGUE G, KORSGREN O, NILSSON B. Low molecular weight dextran sulfate prevents the instant blood-mediated inflammatory reaction induced by adult porcine islets. Transplantation 2004a; 77: 741.
10. NILSSON B, LARSSON R, HONG J et al. Compstatin inhibits complement and cellular activation in whole blood in two models of extracorporeal circulation. Blood 1998; 92: 1661.
11. BRANDHORST H, BRANDHORST D, HERING BJ, BRETZEL RG. Significant progress in porcine islet mass isolation utilizing liberase HI for enzymatic low-temperature pancreas digestion. Transplantation 1999; 68: 355.
12. KISSANE JM, ROBINS E. The fluorometric measurement of deoxyribonucleic acid in animal tissues with special reference to the central nervous system. J Biol Chem 1958; 233: 184.
13. JOHANSSON H, GOTO M, DUFRANE D et al. Low molecular weight dextran sulfate: a strong candidate drug to block IBMIR in clinical islet transplantation. Am J Transplant 2006; 6: 305.
14. NILSSON EKDAHL K, NILSSON B, PEKNA M, NILSSON UR. Generation of iC3 at the interface between blood and gas. Scand J Immunol 1992; 35: 85.
15. MOLLNES TE, RIESENFELD J, GARRED P et al. A new model for evaluation of biocompatibility: combined determination of neoepitopes in blood and on artificial surfaces demonstrates reduced complement activation by immobilization of heparin. Artif Organs 1995; 19: 909.
16. KATRAGADDA M, MAGOTTI P, SFYROERA G, LAMBRIS JD. Hydrophobic effect and hydrogen bonds account for the improved activity of a complement inhibitor, compstatin. J Med Chem 2006; 49: 4616.
17. FERNANDEZ LA, HATCH EW, ARMANN B et al. Validation of large particle flow cytometry for the analysis and sorting of intact pancreatic islets. Transplantation 2005; 80: 729.
18. GOTO M, GROTH CG, NILSSON B, KORSGREN O. Intraportal pig islet xenotransplantation into athymic mice as an in vivo model for the study of the instant blood-mediated inflammatory reaction. Xenotransplantation 2004b; 11: 195.
19. ROOD PP, BOTTINO R, BALAMURUGAN AN et al. Reduction of early graft loss after intraportal porcine islet transplantation in monkeys. Transplantation 2007; 83: 202.
20. PRATT JR, BASHEER SA, SACKS SH. Local synthesis of complement component C3 regulates acute renal transplant rejection. Nat Med 2002; 8: 582.
21. CHOWDHURY P, ZHOU W, SACKS SH. Complement in renal transplantation. Nephron Clin Pract 2003; 95: c3.
22. PENG Q, LI K, PATEL H, SACKS SH, ZHOU W. Dendritic cell synthesis of C3 is required for full T cell activation and development of a Th1 phenotype. J Immunol 2006; 176: 3330.
23. BROWN KM, KONDEATIS E, VAUGHAN RW et al. Influence of donor C3 allotype on late renal-transplantation outcome. N Engl J Med 2006; 354: 2014.
24. OZMEN L, EKDAHL KN, ELGUE G, LARSSON R, KORSGREN O, NILSSON B. Inhibition of thrombin abrogates the instant blood-mediated inflammatory reaction triggered by isolated human islets: possible application of the thrombin inhibitor melagatran in clinical islet transplantation. Diabetes 2002; 51: 1779.
25. HAMAD O, NILSSON EKDAHL K, NILSSON P et al. Complement activation is triggered by chondroitin sulfate released by thrombin receptor activated platelets. J Thrombosis Haemostasis 2008, in press.
26. FIORANTE P, BANZ Y, MOHACSI PJ et al. Low molecular weight dextran sulfate prevents complement activation and delays hyperacute rejection in pig-to-human xenotransplantation models. Xenotransplantation 2001; 8: 24.
27. THOMAS H, MAILLET F, LETOURNEUR D, JOZEFONVICZ J, FISCHER E, KAZATCHKINE MD. Sulfonated dextran inhibits complement activation and complement-dependent cytotoxicity in an in vitro model of hyperacute xenograft rejection. Mol Immunol 1996; 33: 643.
28. SOULIKA AM, KHAN MM, HATTORI T et al. Inhibition of heparin/protamine complex-induced complement activation by Compstatin in baboons. Clin Immunol 2000; 96: 212.

doi:10.1093/brain/awr038 Brain 2011: 134; 1089–1100 | 1089

BRAIN
A JOURNAL OF NEUROLOGY

^{18}F-THK523: a novel *in vivo* tau imaging ligand for Alzheimer's disease

Michelle T. Fodero-Tavoletti,[1,2] Nobuyuki Okamura,[3] Shozo Furumoto,[3] Rachel S. Mulligan,[4] Andrea R. Connor,[1,2] Catriona A. McLean,[5] Diana Cao,[6] Angela Rigopoulos,[6] Glenn A. Cartwright,[6] Graeme O'Keefe,[4] Sylvia Gong,[4] Paul A. Adlard,[1,7] Kevin J. Barnham,[1,2,7] Christopher C. Rowe,[4] Colin L. Masters,[7] Yukitsuka Kudo,[8] Roberto Cappai,[1,2] Kazuhiko Yanai[3] and Victor L. Villemagne[4,7]

1 Department of Pathology, The University of Melbourne, Victoria, 3010, Australia
2 Bio21 Molecular and Biotechnology Institute, The University of Melbourne, Victoria, 3010, Australia
3 Department of Pharmacology, Graduate School of Medicine, Tohoku University, Sendai, 980-8575, Japan
4 Department of Nuclear Medicine and Centre for PET, University of Melbourne, Austin Health, Victoria, 3084, Australia
5 Department of Anatomical Pathology, The Alfred Hospital, Victoria, 3181, Australia
6 Ludwig Institute for Cancer Research, Austin Hospital, Victoria, 3084, Australia
7 The Mental Health Research Institute, Victoria, 3010, Australia
8 Innovation of New Biomedical Engineering Centre, Tohoku University, Sendai, 980-8575, Japan

Correspondence to: Victor L. Villemagne,
Austin Health, Department of Nuclear Medicine and Centre for PET,
145 Studley Road,
Heidelberg,
VIC, 3084, Australia
E-mail: villemagne@petnm.unimelb.edu.au

While considerable effort has focused on developing positron emission tomography β-amyloid imaging radiotracers for the early diagnosis of Alzheimer's disease, no radiotracer is available for the non-invasive quantification of tau. In this study, we detail the characterization of ^{18}F-THK523 as a novel tau imaging radiotracer. *In vitro* binding studies demonstrated that ^{18}F-THK523 binds with higher affinity to a greater number of binding sites on recombinant tau (K18ΔK280) compared with β-amyloid$_{1-42}$ fibrils. Autoradiographic and histofluorescence analysis of human hippocampal serial sections with Alzheimer's disease exhibited positive THK523 binding that co-localized with immunoreactive tau pathology, but failed to highlight β-amyloid plaques. Micro-positron emission tomography analysis demonstrated significantly higher retention of ^{18}F-THK523 (48%; $P < 0.007$) in tau transgenic mice brains compared with their wild-type littermates or APP/PS1 mice. The preclinical examination of THK523 has demonstrated its high affinity and selectivity for tau pathology both *in vitro* and *in vivo*, indicating that ^{18}F-THK523 fulfils ligand criteria for human imaging trials.

Keywords: tau; imaging; Alzheimer's disease; dementia; PET
Abbreviations: PiB = Pittsburgh Compound-B

Introduction

The clinical diagnosis of neurodegenerative diseases such as Alzheimer's disease is typically based on progressive cognitive impairments while excluding other diseases. However, clinical diagnosis is often challenging, with patients presenting with mild and non-specific symptoms attributable to diverse and overlapping pathologies that present as similar phenotypes (van der Zee *et al.*,

Received September 23, 2010. Revised December 21, 2010. Accepted January 10, 2011
© The Author (2011). Published by Oxford University Press on behalf of the Guarantors of Brain. All rights reserved.
For Permissions, please email: journals.permissions@oup.com

Downloaded from brain.oxfordjournals.org at Tohoku University on May 5, 2011

2008). Consequently, definitive diagnosis of neurodegenerative diseases is still reliant on post-mortem examination.

Post-mortem examination of the Alzheimer's disease brain is characterized by gross cortical atrophy (Wenk, 2003). Microscopically, Alzheimer's disease is characterized by the presence of extracellular β-amyloid plaques and intracellular neurofibrillary tangles (Wisniewski *et al.*, 1989; Ho *et al.*, 1994). There has been much progress in developing PET imaging radiotracers for the non-invasive detection of β-amyloid deposition (Shoghi-Jadid *et al.*, 2002; Klunk *et al.*, 2005; Rowe *et al.*, 2007, 2008; Choi *et al.*, 2009). Recent reports indicate that the best characterized and successful imaging agent Pittsburgh Compound-B (PiB), preferentially binds to fibrillar β-amyloid contained within cored and compact plaques (Klunk *et al.*, 2004; Maeda *et al.*, 2007; Ikonomovic *et al.*, 2008) and with much lower affinity to the oligomeric forms of β-amyloid (Maezawa *et al.*, 2008) that are thought to be the toxic species of β-amyloid in Alzheimer's disease (Lambert *et al.*, 2001; Walsh *et al.*, 2002; Ferreira *et al.*, 2007; Cairns *et al.*, 2009).

While amyloid imaging PET studies confirmed that β-amyloid deposition occurs well before the onset of symptoms (supporting the hypothesis that this represents preclinical Alzheimer's disease), these studies also showed the lack of correlation between β-amyloid plaque deposition and cognitive impairment in Alzheimer's disease; suggesting that markers for different and downstream effects of β-amyloid may be better suited to assess disease progression (Jack *et al.*, 2010). Therefore, new ligands are needed to explore alternative biomarkers as specific indicators of neurodegeneration. Such agents may prove invaluable in the diagnosis, follow-up and therapeutic monitoring of Alzheimer's disease and other dementias.

An obvious biomarker is tau and in particular, abnormal deposits of hyperphosphorylated tau as neurofibrillary tangles, neuropil threads and as dystrophic neurites surrounding β-amyloid plaques (a pathological hallmark of Alzheimer's disease); however, tau deposits are also characteristic of a larger group of neurodegenerative diseases termed tauopathies [i.e. sporadic corticobasal degeneration, progressive supranuclear palsy, Picks disease, as well as frontotemporal dementia and parkinsonism linked to chromosome 17 (FTDP-17)] (Lee *et al.*, 2001). Unlike β-amyloid plaque deposition, human post-mortem studies indicate that neurofibrillary tangle density correlates with neurodegeneration and cognitive impairment (Duyckaerts *et al.*, 1987, 1990; Delaere *et al.*, 1989; Arriagada *et al.*, 1992; Dickson, 1997; McLean *et al.*, 1999). Futhermore, abundant neurofibrillary tangles are not observed in cognitively unimpaired individuals, in contrast to β-amyloid plaques that are present in some non-demented people (Katzman *et al.*, 1988; Delaere *et al.*, 1990; Rowe *et al.*, 2007, 2008). Moreover, CSF-tau and phospho-tau (ptau181) have been proven useful biomarkers in the diagnosis of Alzheimer's disease (Blennow and Hampel, 2003; Ganzer *et al.*, 2003; Hampel *et al.*, 2009*a*, *b*).

Despite the quantitative assessment of CSF levels of tau and phospho-tau being reliable biomarkers of neurodegeneration (Jack *et al.*, 2010), lumbar puncture is an invasive procedure for the widespread screening of the at-risk population. Additionally, CSF measures do not provide information on regional brain tau deposition that may have clear correlates with cognition (i.e. hippocampus) and therefore, might not be able to provide important information on the therapeutic outcomes or response to current drugs aimed at modulating tau/neurofibrillary tangles (Gozes *et al.*, 2009; Hampel *et al.*, 2009*a*, *b*; Wischik and Staff, 2009).

Molecular neuroimaging with tau-specific radiotracers may provide highly accurate, reliable and reproducible quantitative statements of global and regional brain tau burden, essential for the evaluation of disease progression, therapeutic trial recruitment and the evaluation of tau-specific therapeutics (for both Alzheimer's and non-Alzheimer's disease taupathies); where tau plays a central role. Certainly, the viability of imaging disease-specific traits has been demonstrated in recent years by PET ligands such as ^{11}C-PiB (Klunk *et al.*, 2004) and ^{18}F-FDDNP, used for imaging β-amyloid deposition. Unlike PiB, it has been suggested that FDDNP also binds to neurofibrillary tangles (Agdeppa *et al.*, 2001), which may contribute to ^{18}F-FDDNP retention in the mesial temporal cortex where β-amyloid-specific tracers such as ^{11}C-PiB scarcely bind (Kepe *et al.*, 2006; Ng *et al.*, 2007; Pike *et al.*, 2007; Rowe *et al.*, 2007).

Okamura and colleagues (2005) screened over 2000 small molecules to develop novel radiotracers with high affinity and selectivity for tau pathology/neurofibrillary tangles. Consequently, they identified a series of novel quinoline and benzimidazole derivatives that bind neurofibrillary tangles and, to a lesser extent, β-amyloid plaques. Serial analysis of those compounds led to the design and synthesis of a novel imaging agent, ^{18}F-THK523. The purpose of this study was to utilize a series of *in vitro*, *ex vivo* and *in vivo* techniques to determine whether ^{18}F-THK523 satisfied a number of radioligand criteria, assessing its suitability for the quantitative imaging of tau pathology in the human brain.

Materials and methods

Materials

All reagents were purchased from Sigma, unless otherwise stated. Human β-amyloid$_{1-42}$ was purchased from the W. M. Keck Laboratory (Yale University).

Mice

Mice were housed in conditions of controlled temperature (22 ± 2°C) and lighting (14:10 h light–dark cycle) with free access to food and water. rTg(TauP301L)4510 and their wild-type (CamKII) littermates were a kind gift from Jada Lewis (Dept Neuroscience, Mayo Clinic, Florida, USA) and APP/PS1 [B6C3-Tg(APPswe, PSEN1dE9)85Dbo/J] and wild-type littermates were purchased from JAX® Mice and Services. MicroPET studies employed 6-month-old rTg(TauP301L)4510 mice and 12-month-old APP/PS1 [B6C3-Tg(APPswe, PSEN1dE9)85Dbo/J] mice and their respective wild-type littermates.

Tissue collection and characterization

Human brain tissue was collected at autopsy. The sourcing and preparation of the human brain tissue was conducted by the Victorian Brain Bank Network. Alzheimer's disease pathological diagnosis was made according to standard NIA-Reagan Institute criteria (1997).

Downloaded from brain.oxfordjournals.org at Tohoku University on May 5, 2011

Determination of age-matched control cases were subject to the above criteria. Three Alzheimer's disease and three healthy, age-matched control cases were examined in this study.

^{18}F-labelling of THK523

Unlabelled THK523 and 2-(4-aminophenyl)-6-(2-tosyloxyethoxy)quinoline (BF241; the precursor for ^{18}F-THK523) were custom synthesized by Tanabe R&D Service Co. and confirmed for purity by reverse phase high-performance liquid chromatography, 1D nuclear magnetic resonance and mass spectrometry. ^{18}F-THK523 (Fig. 1) was synthesized by nucleophilic substitution of the tosylate precursor (BF-241). Following a 10-min reaction at 110°C, the crude reaction was partially purified on an activated Sep-Pak tC18 cartridge before undergoing semi-preparative reverse phase high-pressure liquid chromatography purification. Standard tC18 Sep-Pak reformulation produced ^{18}F-THK523 in >95% radiochemical purity. The radiochemical yield was 24% (non-decay corrected) and at end of synthesis, the average specific activity was 100 GBq/μmol (2.7Ci/μmol).

Measurement of octanol/water partition coefficient

^{18}F-THK523 (37 MBq) was added to a mixture of 3 ml 1-octanol and 3 ml of 1 M potassium phosphate buffer (pH 7.4). The mixture was shaken for 30 min, followed by centrifugation for 3 min. Aliquots (0.5 ml) were carefully taken from each phase for assay. The partition coefficient was calculated as follows: (count per minute/0.5 ml l-octanol)/(count per minute/0.5 ml buffer). Measurements were done in triplicate.

Generation and protein purification of K18Δ280 K-tau

K18Δ280 K-tau is a fragment of the full length protein, htau40 (Barghorn *et al.*, 2004; von Bergen *et al.*, 2006) comprising the four repeat regions of tau including residues 243–372. Polymerase chain reaction was implemented to generate K18Δ 280 K-tau from plasmids kindly provided by the Mayo Clinic. Δ280K refers to the deletion of the lysine residue at position 280. DNA encoding this region was cloned into expression vector pET15b at the NcoI and XhoI sites and transfected into BL21DE3 *Escherichia coli*. Ampicillin selected *E. coli* were lysed in buffer comprising 50 mM PIPES pH 6.9, 1 mM EDTA, 5 mM dithiothreitol and protease inhibitor cocktail (Roche), sonicated on ice (6 × 30 min, with 30 s rest intervals) and the lysate was then spun at 18 000*g* at 4°C for 15 min. The supernatant was removed and added to a solution of NaCl at a final concentration of 0.5 M. The sample was then boiled for 20 min prior to centrifugation using the abovementioned conditions. The supernatant was then applied to a PD10 column (Amersham) and equilibrated in equilibration buffer (50 mM Tris pH 8.2, 20 mM NaCl, 1 mM EDTA, 5 mM dithiothreitol) and filtered prior addition to a SP sepharose column. Protein fractions were then analysed by Coomassie staining and western blot and appropriate fractions containing a single tau band were pooled, buffer exchanged into water (PD10), lyophilized and stored at −80°C.

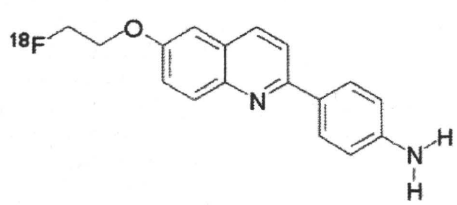

Figure 1 Chemical structure of ^{18}F-THK523 [2-(4-aminophenyl)-6-(2-fluoroethoxy)quinoline)].

Preparation of β-amyloid$_{1–42}$ and tau fibrils

Synthetic β-amyloid$_{1–42}$ was dissolved in 1 × phosphate buffered saline pH 7.7 to a final concentration of 200 μM. K18Δ280K-tau was dissolved in 1 × phosphate buffered saline pH 7.4 buffer to a final concentration of 20 μM. The solutions were then incubated at 37°C for 2 and 3 days, respectively, with agitation at 220 and 800 rpm, respectively (Orbital mixer incubator, Ratek). β-amyloid$_{1–42}$ fibril aggregation was confirmed via thioflavin T fluorescence spectroscopy and tau aggregation was confirmed by thioflavin S fluorescence spectroscopy; both fibril preparations were examined by transmission electron microscopy.

Thioflavin S/thioflavin T fluorescence

Aggregation of β-amyloid$_{1–42}$ fibril was confirmed using thioflavin T fluorescence (LeVine, 1999). Reactions (100 μl) comprising 20 μM β-amyloid$_{1–42}$ fibrils, 10 μM thioflavin T, 50 mM phosphate buffer were analysed at 444 nm (excitation) and 450–550 nm (emission), with an integration time of 1 s. K18Δ280K-tau fibril formation was confirmed by thioflavin S fluorescence whereby reactions comprising K18Δ280K-tau fibrils, 0.005% thioflavin S in 1 × phosphate buffered saline pH 7.4 were analysed at 440 nm (excitation) and 480 nm (emission), with an integration time of 1 s. Measurements were recorded using a Varian fluorescence spectrophotometer.

Transmission electron microscopy

Fibril formation of β-amyloid$_{1–42}$ and K18Δ280K-tau was further confirmed by transmission electron microscopy following staining with uranyl acetate. Carbon-coated copper electron microscopy grids were coated with K18Δ280K-tau or β-amyloid$_{1–42}$ fibrils, as described previously (Smith and Radford, 2001). Grids were viewed on a Siemens 102 transmission electron microscope, operating at a voltage of 60 kV.

In vitro ^{18}F-THK523 binding assays

Synthetic β-amyloid$_{1–42}$ or K18Δ280K-tau fibrils (200 nM) were incubated with increasing concentrations of ^{18}F-THK523 (1–500 nM). To account for non-specific binding of ^{18}F-THK523, the reactions described above were duplicated in the presence of unlabelled 1 μM THK523. The binding reactions were incubated for 1 h at room temperature in 200 μl of assay buffer [phosphate buffered saline, minus Mg^{2+} and Ca^{2+} (JRH Biosciences); 0.1% bovine serum albumin]. Separation of bound from free radioactivity was achieved by filtration under reduced pressure (MultiScreen HTS Vacuum Manifold; Multiscreen HTS 96-well filtration plates; 0.65 μm, Millipore). Filters were washed three times with 200 μl assay buffer and the radioactivity contained within the filters was counted in a γ-counter (Wallac 1480 Wizard 3"; Perkin Elmer). Binding data were analysed with curve fitting software that calculates the K_D and B_{max} using non-linear regression (GraphPad Prism Version 1.0, GraphPad Software). All experiments were conducted in triplicate.

Downloaded from brain.oxfordjournals.org at Tohoku University on May 5, 2011

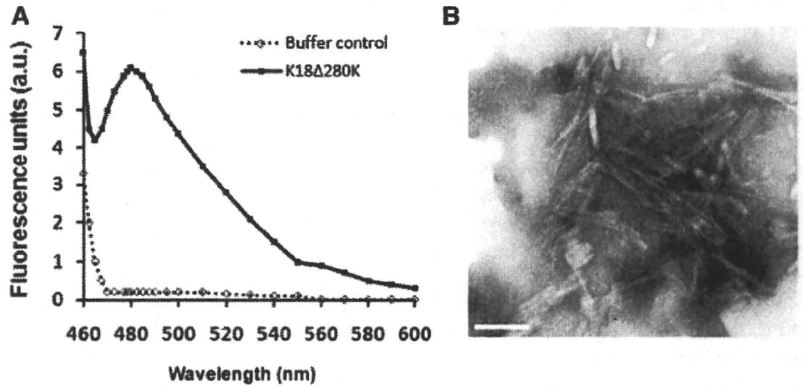

Figure 2 Characterization of K18Δ280K-tau fibrils. Recombinant K18(Δ280K)-tau was incubated with agitation (800 rpm) for 3 days at 37°C. (**A**) Graph depicting thioflavin S fluorescence, excitation/emission 440/480 nm, for K18Δ280K-tau (solid line) and no tau buffer control (dotted line). The graph for K18Δ280K-tau is indicative of positive amyloid fibril formation. (**B**) Electron microscopy image of K18Δ280K-tau fibrils. TechaniG^2 electron microscope; ×59 000 magnification. Scale bar: 50 nm. These data are representative of three independent experiments. a.u. = arbitrary units.

Immunohistochemistry and fluorescence analysis

Brain tissue from Alzheimer's disease and healthy control cases [three Alzheimer's disease (two female, one male), age range 75–83 years; three healthy controls (three female), age range 72–85 years], as well as mice (rTg4510, APP/PS1 and wild-type littermates) was fixed in 10% formalin/phosphate buffered saline and embedded in paraffin. For immunohistochemistry, 5 µm serial sections were deparaffinized and treated with 80% formic acid for 5 min and endogenous peroxidase activity was blocked with 3% hydrogen peroxide. Sections were then treated with blocking buffer (20% foetal calf serum, 50 mM Tris–HCl, 175 mM NaCl pH 7.4) before incubation with primary antibodies to β-amyloid (1E8; 1:50) or tau pAb (DAKO), for 1 h at room temperature. Serial 5 µm tissue sections were stained as follows: the first and third sections were immunostained with tau or 1E8 antibodies to identify tau tangles or β-amyloid plaques, respectively. The second serial section was stained with unlabelled THK523 to assess whether THK523 staining co-localized with the immunodetected tau tangles and/or β-amyloid plaques. Visualization of antibody reactivity was achieved with the LSAB™ kit (labelled streptavidin-biotin, DAKO) and sections were then incubated with hydrogen peroxidase-diaminobenzidine (H_2O_2-DAB) to visualize the tau tangles or β-amyloid-positive deposits. Sections were counterstained with Mayer's haematoxylin. To detect THK523 fluorescence, quenching was first performed whereby sections were first deparaffinized and tissue autofluorescence minimized by treatment of sections with 0.25% $KMnO_4$/phosphate buffered saline for 20 min prior to washing (phosphate buffered saline) and incubation with 1% potassium metabisulphite/1% oxalic acid/phosphate buffered saline for 5 min. Following autofluorescence quenching, sections were blocked in 2% bovine serum albumin/phosphate buffered saline pH 7.0 for 10 min and stained with 100 µM THK523 for 30 min. Washed (phosphate buffered saline) sections were then mounted in non-fluorescent mounting media (DAKO). Epifluorescence images were visualized on a Zeiss microscope [47CFP; filter set 47 (EM BP 436/20, BS FT 455, EM BP480/40)]. Co-localization of the THK523 and antibody signals was assessed by overlaying images from each of the stained serial tissue sections.

Autoradiography

For autoradiography, the hippocampal brain section of a patient with Alzheimer's disease (90-year-old female) was incubated with 2.2 MBq/ml of ^{18}F-THK523 at room temperature for 10 min and then washed briefly with water and 50% ethanol. After drying, the labelled section was exposed to a BAS-III imaging plate (Fuji Film) overnight. Autoradiographic images were obtained using a BAS-5000 phosphor imaging instrument (Fuji Film) with a spatial resolution of 25 × 25 µm. Neighbouring sections were immunostained using AT8 anti-tau monoclonal antibody (Innogenetics; diluted 1:20) or 6F/3D anti-Aβ antibody (DAKO; diluted 1:50).

Ex vivo biodistribution of ^{18}F-THK523

^{18}F-THK523 (0.68–1.32 MBq) was administered into the tail vein of ICR mice (n = 20, male, average weight 28–32 g). The mice were then sacrificed by decapitation at 2, 10, 30, 60 and 120 min post injection. The brain, blood and other organs were removed and weighed, and the radioactivity was counted with an automatic γ-counter. The percentage injected dose per gram (%ID/g) was calculated by comparison of tissue count to tissue weight. Each %ID/g value is an average ± SD of four separate experiments.

Small animal positron emission tomography imaging

All PET scans were conducted using a Philips MOSAIC small animal PET scanner with a transaxial spatial resolution of 2.7 mm full-width at half-maximum. Mice [n = 8 rTg4510 (four females, four males), n = 7 wild-type (four females, three males) mice and n = 3 APP/PS1 (all females) and three of their wild-type littermates (all females)] were intravenously injected with 100 µl of radiotracer comprising 3.7 MBq (0.35 µg/kg) of ^{18}F-THK523 via the tail vein. Mice were then anaesthetized using an isoflurane vaporizer with oxygen flow metre set to 5 l/min/5% isoflurane. Anaesthesia was maintained in a Veterinaire MINERVE anaesthetic assembly with the oxygen flow metre set to 2 l/min and vaporizer setting at 2%. A series of 6 × 5-min dynamic

Downloaded from brain.oxfordjournals.org at Tohoku University on May 5, 2011

emission scans were acquired starting at 5 min after injection. All images were reconstructed using a 3D row action maximum likelihood algorithm (RAMLA). Summed 25–35 min post-injection images were used for comparison between transgenic and wild-type mice. Image analysis was conducted using Wasabi v.2.0 software.

Statistical analysis

Normality of distribution was tested using the Shapiro–Wilk test and visual inspection of variable histograms. Statistical evaluations to assess differences in ^{18}F-THK523 binding were performed with analysis of variance (ANOVA) and a Tukey–Kramer Honestly Significant Difference test to establish differences between group means. Data are presented as mean ± SD unless otherwise stated.

Results

^{18}F-THK523 exhibits high affinity and selectivity for recombinant tau fibrils

To determine whether ^{18}F-THK523 satisfied the criteria of high affinity and selectivity for tau, the binding properties of ^{18}F-THK523 to tau fibrils was investigated and compared with β-amyloid$_{1-42}$ fibrils. A previously described truncated mutant of human tau, termed K18Δ280K-tau (Barghorn *et al.*, 2004; von Bergen *et al.*, 2006) that comprises the C-terminus of tau, including the four repeat regions and the FTDP-17 tau gene deletion resulting in the omission of lysine at position 280 (denoted Δ280K) was used for the studies. K18Δ280K-tau aggregates at low micromolar concentrations into paired helical filaments and straight filaments in the presence and absence of heparin (Perez *et al.*, 1996). Prior to conducting the binding assays, K18Δ280K-tau was formed into fibrillar structures (as monitored by thioflavin S fluorescence and transmission electron microscopy) by incubating 20 μM protein over 3 days at 37°C. On day 3, K18Δ280K-tau showed a thioflavin S fluorescence signal at ~480 nm (Fig. 2A), indicative of positive fibril formation. Fibril formation was confirmed by transmission electron microscopy with uranyl acetate staining (Fig. 2B). The β-amyloid$_{1-42}$ fibrils were generated as previously described (Fodero-Tavoletti *et al.*, 2007).

In vitro saturation studies were conducted using equimolar concentrations (200 nM, ~4.0×10^{-11} moles) of either K18Δ280-tau or β-amyloid$_{1-42}$ fibrils. While two classes of binding sites were identified on K18Δ280-tau fibrils (Fig. 3A) only one class of ^{18}F-THK523 binding sites was identified on β-amyloid$_{1-42}$ fibrils (Fig. 3B). Furthermore, there was a 10-fold higher affinity of ^{18}F-THK523 for the first class of K18Δ280-tau binding sites compared with β-amyloid$_{1-42}$ fibrils (Table 1). Overall, there was a ~5-fold higher number of ^{18}F-THK523 binding sites (B_{max}) on K18Δ280-tau fibrils, compared with β-amyloid$_{1-42}$ fibrils (Table 1).

THK523 demonstrates selectivity for tau pathology in sections of human hippocampal tissue

As a qualitative measure of its selectivity for tau pathology, THK523 recognition of tau pathology was assessed by histofluorescence and autoradiography. ^{19}F-THK523 and ^{18}F-THK523 share the same chemical structure, although ^{19}F is substituted for ^{18}F in the radiolabelled compound. For histofluorescence, unlabelled

Table 1 Binding parameters of ^{18}F-THK523 binding to fibrils

	K_{D1}	B_{max1}	K_{D2}	B_{max2}
K18Δ280K-tau fibrils	1.67	2.20	21.74	4.46
β-amyloid$_{1-42}$ fibrils	20.7	1.25		

K_D are in nM and B_{max} are in pmol ^{18}F-THK523/nmol fibrils.

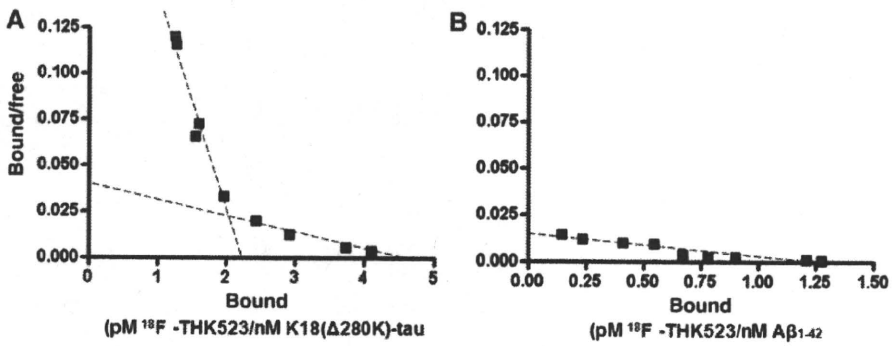

Figure 3 *In vitro* binding studies indicate two classes of ^{18}F-THK523-binding sites on K18Δ 280K-tau fibrils. Scatchard plots of ^{18}F-THK523 binding to synthetic K18Δ280K-tau (**A**) or (**B**) β-amyloid$_{1-42}$ fibrils. (**A**) Scatchard analysis identified two classes of THK523 binding sites on K18Δ280K-tau fibrils (K_{D1} and B_{max1} of 1.67 nM and 2.20 pmol THK523/nmol K18Δ280 K-tau, respectively; K_{D2} and B_{max2} of 21.7 nM and 4.46 pmol THK523/nmol K18Δ280 K-tau, respectively). (**B**) Scatchard analysis identified one class of THK523 binding sites on β-amyloid$_{1-42}$ with K_D and B_{max} of 20.7 nM and 1.25 pmol THK523/nmol β-amyloid$_{1-42}$. Binding data were analysed using GraphPad Software (Version 1.0). These data are the mean of three experiments for K18Δ280 K-tau and four experiments for β-amyloid fibrils.

Downloaded from brain.oxfordjournals.org at Tohoku University on May 5, 2011

THK523 binding to fixed serial sections from the hippocampus of subjects with Alzheimer's disease and age-matched controls was assessed. Contiguous sections were immunostained for β-amyloid and tau pathology with anti-β-amyloid and anti-tau antibodies, respectively. In all tissue sections examined, positive THK523 staining co-localized with tau pathology as detected in the contiguous tau immunostained section assessed (Fig. 4). THK523 failed to bind to diffuse β-amyloid plaques as indicated by the lack of co-localization with immunodetected β-amyloid pathology (Fig. 4). Likewise, autoradiography analysis in Alzheimer's disease hippocampal sections demonstrated that ^{18}F-THK523 bound to tau pathology with no ^{18}F-THK523 co-localization with immunodetected β-amyloid plaques (Fig. 5).

^{18}F-THK523 crosses the blood–brain barrier in mice

As well as being of low molecular weight (282.31 g/mol) and amenable to labelling with ^{18}F at high specific radioactivity [100 GBq/μmol (2.7 Ci/μmol)], a tau radiotracer should be adequately lipophilic to be able to cross the blood–brain barrier. The octanol/water coefficient ($logP_{oct}$) of ^{18}F-THK523 as a measure of lipophilicity, was calculated to be 2.91 ± 0.13. *Ex vivo* biodistribution studies of ^{18}F-THK523 in ICR mice, measured at 2, 10, 30, 60 and 120 min post injection, showed brain peak uptake of 2.75 ± 0.25% ID/g at 2 min post-intravenous injection (Fig. 6), indicating that ^{18}F-THK523 has adequate lipophilicity to cross the blood–brain barrier.

In vivo retention of ^{18}F-THK523 is significantly higher in tau transgenic mice brain compared with control and APP/PS1 mice

To further characterize ^{18}F-THK523 as a tau imaging radiotracer, *in vivo* microPET studies were performed to compare the retention of ^{18}F-THK523 in tau transgenic mice (rTg4510), versus their wild-type littermates (CamKII). Four independent studies were undertaken with 15 mice ($n = 8$ rTg4510 and $n = 7$ CamKII).

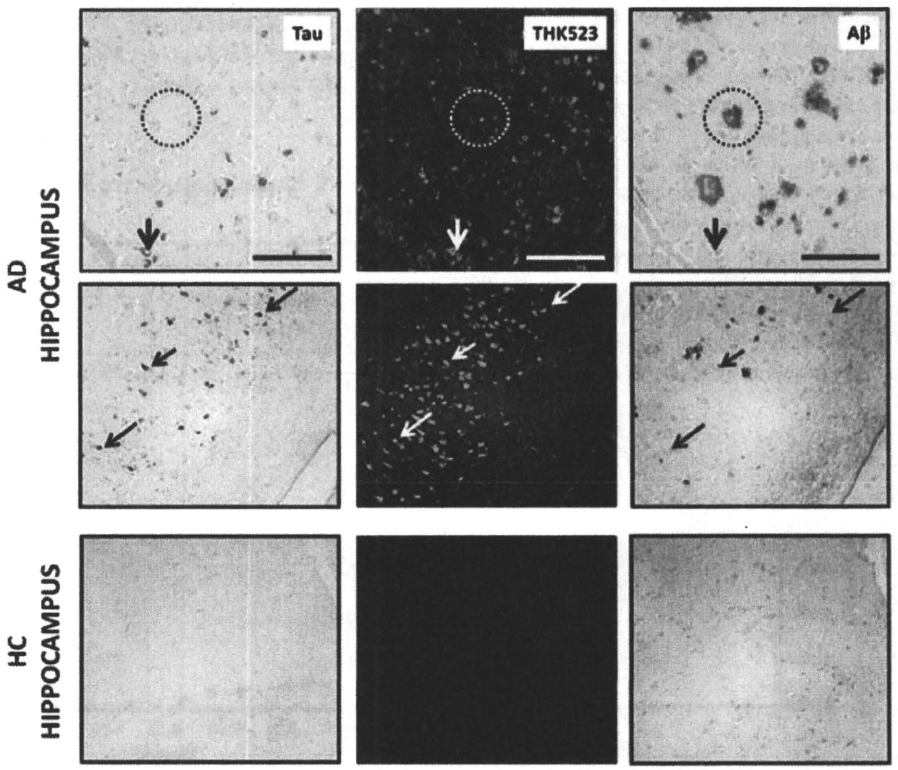

Figure 4 Histofluorescence analysis indicates that THK523 binds specifically to tau tangles with no detectable binding to β-amyloid plaques. Microscopy images of three serial sections (5 μm) from the hippocampus of a patient with Alzheimer's disease (AD) (*top* and *middle*) and a healthy control (HC) (*bottom*), immunostained with antibodies against tau (DAKO) and β-amyloid (1E8), to identify tau tangles and β-amyloid (Aβ) plaques, respectively; or stained with 100 μM THK523. Arrows indicate the location of tau tangles, while circles indicate the location of β-amyloid plaques. Positive THK523 staining appears to co-localize with tau immunostaining of neurofibrillary tangles in the hippocampus sections examined, but not to plaques. Tissue sections were imaged using a Zeiss microscope and Axiocam digital camera. Scale bars: 100 μm (*top*) and 200 μm (*middle* and *bottom*). These figures are representative of three subjects with Alzheimer's disease (two females, one male, age range 75–83 years) and three healthy controls (all female, age range 72–85 years).

Downloaded from brain.oxfordjournals.org at Tohoku University on May 5, 2011

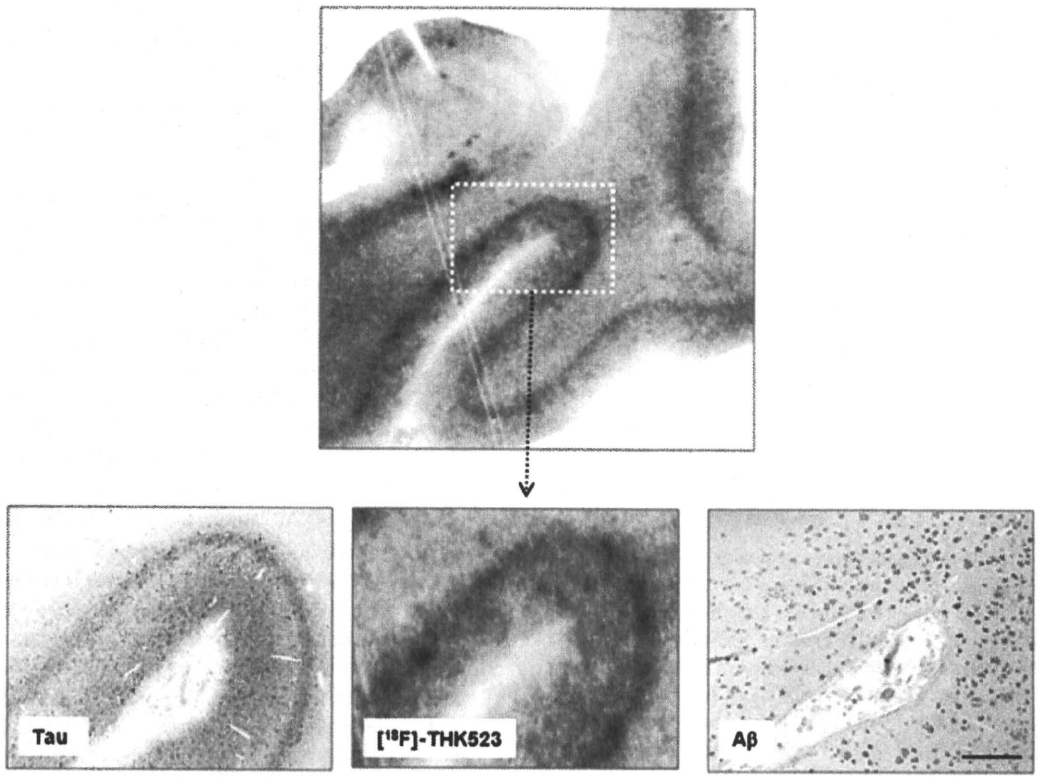

Figure 5 Autoradiography analysis indicates that ^{18}F-THK523 binds specifically to tau tangles with no detectable binding to β-amyloid plaques. (*Top*) ^{18}F-THK523 autoradiogram of Alzheimer's disease hippocampus (90-year-old female) serial section (low magnification). *Bottom*: microscopy images and autoradiogram (higher magnification) images of three serial sections (5 μm) from the hippocampus of the same Alzheimer's disease brain, immunostained with antibodies to tau (AT8, Innogenetics) and β-amyloid (6F/3D, DAKO), to identify tau tangles and β-amyloid (Aβ) plaques, respectively; or labelled with 2.2 MBq/ml ^{18}F-THK523. Positive ^{18}FTHK523 labelling appears to co-localize with tau immunostaining of neurofibrillary tangles in the hippocampus sections examined, but not to plaques. Scale bars: 500 μm. Autoradiographic images were obtained using a BAS-5000 phosphor imaging instrument (Fuji Film).

Representative microPET images are depicted in Fig. 7A and ^{18}F-THK523 time activity curves are depicted in Fig. 7C. Brain retention at ~30 min post injection of ^{18}F-THK523 was significantly higher (48%; $P < 0.007$) in the rTg4510 mice compared with their wild-type littermates (Fig. 7B). Analysis of bone, liver and intestine showed no significant differences in ^{18}F-THK523 retention (Fig. 7B), indicating a specific difference in brain uptake. Following microPET scanning, each mouse was euthanized and brains were harvested for biochemical and histofluorescence analysis. All rTg4510 mice brains examined were positive for tau overexpression as determined by western blot and immunohistochemical analysis (data not shown). Histofluorescence analysis of the same rTg4510 mice assessed by microPET identified positive THK523 staining that co-localized with immunopositive tau deposits (Fig. 8).

To further characterize the *in vivo* selectivity of ^{18}F-THK523 for tau pathology, microPET studies were conducted using the same experimental procedure in APP/PS1 transgenic mice ($n = 3$), exhibiting cerebral β-amyloid pathology but no tau deposits (Holcomb *et al.*, 1999). MicroPET analysis demonstrated that there was significantly lower retention of ^{18}F-THK523 in the brains of APP/PS1 mice, no different from the retention in their wild-type littermates ($n = 3$; Fig. 7B). Importantly, histofluorescence evaluation of rTg4510 and APP/PS1 brain tissue with 10 nM THK523 (a concentration that is achieved in the brain during PET studies), showed binding of THK523 to tau deposits in rTg4510 mice brains with negligible binding to β-amyloid plaques in the brain of APP/PS1 mice (Fig. 8).

Discussion

With the recent advances in instrumentation, image analysis and the development of new brain radiotracers, molecular neuroimaging with PET is rapidly expanding our knowledge base of neurodegenerative disease progression, improving early and accurate diagnosis, while promising to be effective in therapeutic monitoring and aiding in drug discovery and development. To date, much success has been achieved with β-amyloid radiotracers, in particular PiB being the best characterized radiotracer both *in vitro* and *in vivo*; showing selectivity for β-amyloid pathology resulting in a robust difference in ^{11}C-PiB brain retention in Alzheimer's disease

Downloaded from brain.oxfordjournals.org at Tohoku University on May 5, 2011

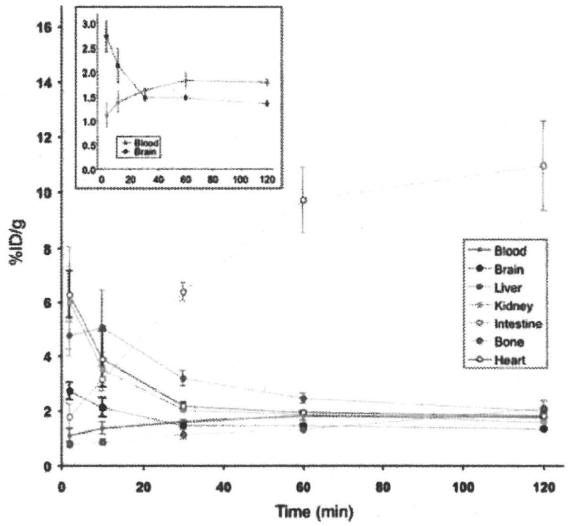

Figure 6 *Ex vivo* biodistribution studies of ^{18}F-THK523 in ICR mice. Initial uptake was highest (~6.2%ID/g) in the heart and kidney followed by a fast clearance. Liver radioactivity peaked (~5.0%ID/g) at 10 min after injection and was followed by a slow clearance, which mirrored a steady and substantial rise in radioactivity in the intestine (11%ID/g at 120 min after injection), suggesting that most of the tracer and/or its metabolites are eliminated through biliary excretion. There was a slow but steady increase in bone radioactivity, reaching a 2.1%ID/g at 120 min after injection, probably indicative of some degree of defluorination. The insert shows in better detail the brain and blood curves. Maximal ^{18}F-THK523 brain uptake (2.75%ID/g) was observed at 2 min after injection of the radiotracer, followed by a rapid clearance from the brain. Radioactivity in blood showed a different kinetic behaviour than the one observed in the brain, with a steady rise in radioactivity reaching an apparent plateau at about 60 min after injection. Uptake at each time point is expressed as percentage of injected dose per body weight (%ID/g) of ^{18}F-THK523. Curve represents the mean ± SD from four independent experiments. A total of 20 mice were examined.

compared with healthy aged-matched individuals in PET studies (Klunk *et al.*, 2004, 2005; Fodero-Tavoletti *et al.*, 2007, 2009). In addition to β-amyloid plaques, Alzheimer's disease brains are also pathologically characterized by the presence of tau pathology. Therefore, tau imaging may improve the specificity of diagnosis, allowing early detection of Alzheimer's disease and Pick's disease, where tau plays a role.

The identification and development of suitable PET radiotracer(s) is a demanding task especially given the considerable number of requirements that a radiotracer should fulfil to be deemed suitable for *in vivo* quantitative brain imaging. This study is the first to report a tau imaging radiotracer (^{18}F-THK523), that satisfies a number of criteria required for quantitative imaging of tau pathology in the human brain (Laruelle *et al.*, 2003; Nordberg, 2004; Pike, 2009). This study has shown that ^{18}F-THK523 has high affinity for recombinant tau fibrils and selectivity for tau fibrils/pathology over β-amyloid fibrils/pathology *in vitro*. Furthermore, it penetrates the blood–brain barrier, selectively highlighting tau pathology in the brains of rTg4510 tau transgenic mice *in vivo*.

In vitro saturation binding studies demonstrated that ^{18}F-THK523 binds to recombinant tau fibrils with high affinity in the low nanomole range. Typically ligands displaying affinities between 0.01–1.00 nM are deemed useful for *in vivo* quantitative PET studies. The high affinity ^{18}F-THK523-binding site (K_{D1}; 1.7 nM) exhibited >10-fold higher affinity compared with β-amyloid$_{1-42}$ fibrils (20.7 nM). Moreover, the number of high affinity ^{18}F-THK523-binding sites (K_{D1}) was almost 2-fold higher than the number of sites on β-amyloid$_{1-42}$ fibrils. In comparison to previous ^{3}H-PiB studies (Klunk *et al.*, 2005; Fodero-Tavoletti *et al.*, 2007), the affinity of ^{3}H-PiB for β-amyloid$_{1-42}$ (K_{D1}, 0.71–0.91 nM) is similar to the affinity of ^{18}F-THK523 for tau fibrils (K_{D1}, 1.7 nM). However, tau fibrils exhibit a larger number of ^{18}F-THK523 binding sites (B_{max1}, 2.20 pmol ^{18}F-THK523/nmol K18Δ280K-tau), compared with what has previously been reported for ^{3}H-PiB and β-amyloid$_{1-42}$ (1.01 pmol PiB/nmol β-amyloid$_{1-42}$) (Fodero-Tavoletti *et al.*, 2007). As the concentration of imaging radiotracers typically achieved during PET studies is in the low nanomole range, these findings strongly suggest that ^{18}F-THK523 will bind with high affinity and selectively to tau pathology under PET imaging conditions. Furthermore, as the brain area occupied by plaques is larger in comparison to neurofibrillary tangles, a >10-fold higher affinity and a larger number of ^{18}F-THK523-binding sites on tau/neurofibrillary tangles over β-amyloid plaques may prove essential in ascertaining a high tau signal over background in human PET studies (Laruelle *et al.*, 2003).

Further evidence of ^{18}F-THK523 selectivity for tau pathology was demonstrated by autoradiography and histofluorescence with positive THK523 staining, co-localizing with tau pathology and not with β-amyloid plaques in human Alzheimer's disease hippocampal sections. Importantly, even at THK523 concentrations 10 000-fold higher than those typically achieved under PET studies, THK523 failed to bind to diffuse plaques in the histofluorescence studies. There was some inconsistent staining of cored/compact plaques, suggesting that there might be some ^{18}F-THK523 binding to cored β-amyloid plaques, but only under non-PET radiotracer conditions. Similarly, variable staining of neurofibrillary tangles at high concentrations of PiB, has been reported by Ikonomovic and colleagues (2008).

In addition to high affinity and selectivity, a suitable tau radiotracer must be able to cross the blood–brain barrier to reach its target *in vivo*. The small size (molecular weight <450) (Laruelle *et al.*, 2003) and lipophilic nature of ^{18}F-THK523 [log P_{OCT} value of 2.9 ± 0.1; −logP_{OCT} values in the range of 0.9 and 3.0, show optimal entry into the brain (Dishino *et al.*, 1983)] indicates that ^{18}F-THK523 is able to penetrate the blood–brain barrier. This was confirmed in both *ex vivo* biodistribution and *in vivo* microPET imaging studies. Additionally, microPET imaging demonstrated that ^{18}F-THK523 retention was significantly higher (48%; $P = 0.007$) in the brains of rTg4510 tau transgenic mice compared with their control littermates, devoid of tau pathology; in agreement with the *in vitro* saturation and histofluorescence studies. Moreover, selectivity of THK523 for tau pathology was further supported by the ^{18}F-THK523 microPET assessment of APP/PS1 mice. These mice possess substantial cerebral β-amyloid plaque

Downloaded from brain.oxfordjournals.org at Tohoku University on May 5, 2011

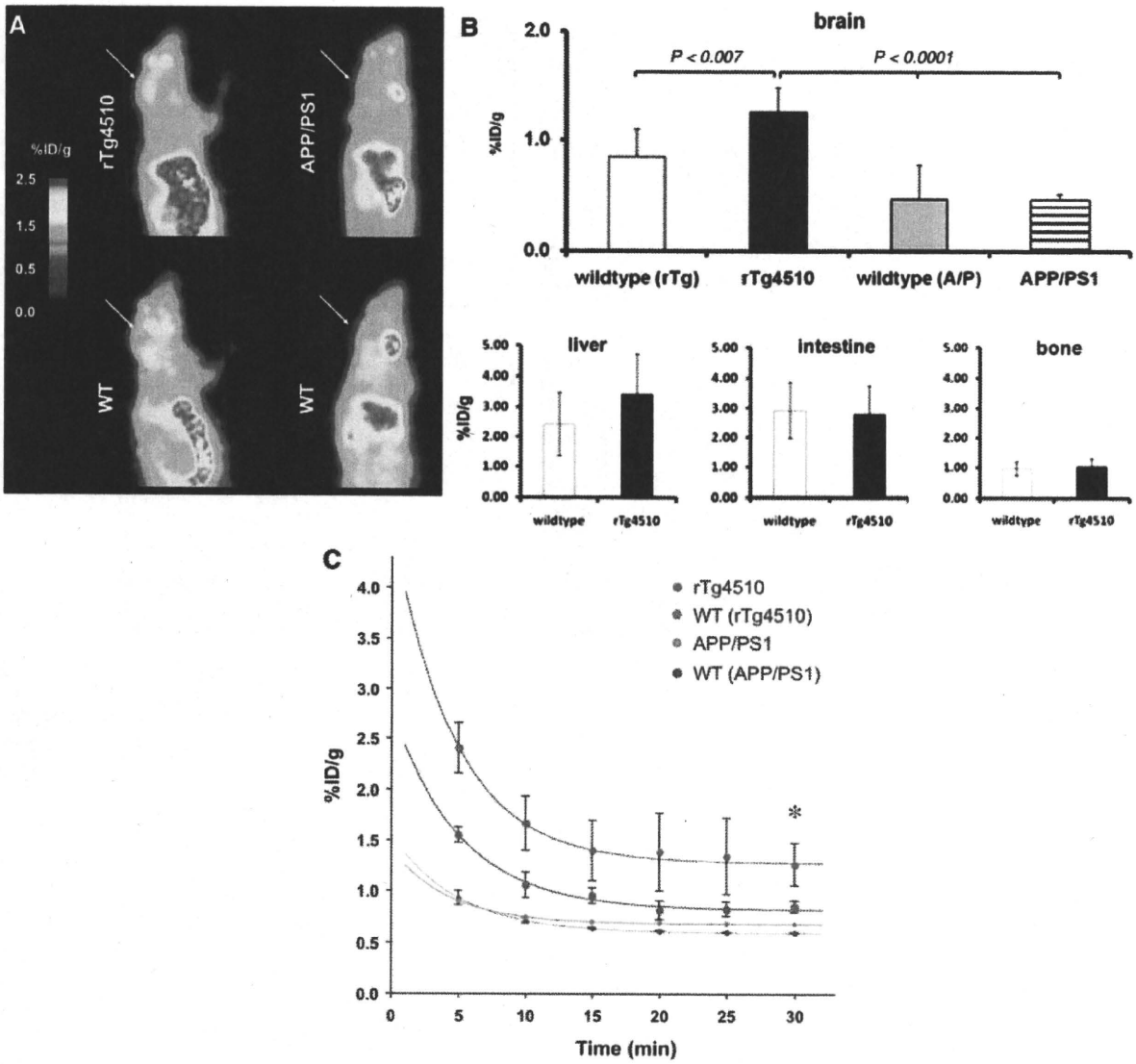

Figure 7 *In vivo* ^{18}F-THK523 microPET studies of tau and β-amyloid overexpressing transgenic mice. (**A**) Representative microPET scans at 30-min post injection of ^{18}F-THK523. rTg4510 mice (*top, left*) exhibited higher ^{18}F-THK523 brain retention compared with their wild-type (WT) littermate (*bottom, left*). Low ^{18}F-THK523 retention was observed APP/PS1 (*top, right*) versus their wild-type littermates (bottom, right). (**B**) Analysis of the ^{18}F-THK523 brain microPET data (30-min post injection) in rTg4510, APP/PS1 mice and their respective wild-type littermates revealed significantly higher (*) retention of ^{18}F-THK523 in the brain (*top*) of rTg4510 mice compared with APP/PS1 mice as well as their respective wild-type littermates. No significant differences in ^{18}F-THK523 retention were observed in the liver, intestine and bone (*bottom*). Data are presented as mean ± SD. (**C**) Brain time-activity curves of ^{18}F-THK523 microPET data expressed as percentage of injected dose per body weight (%ID/g) of ^{18}F-THK523 at each time point. Curve represents the mean ± SD of four independent studies employing $n = 8$ rTg4510 (four females, four males), $n = 7$ WT (four females, three males) mice and $n = 3$ APP/PS1 (all females) and three of the wild-type (all females) mice. Data are presented as mean ± SD.

load; however, the retention of ^{18}F-THK523 in these mice was significantly lower than in rTg4510 tau transgenic mice and not different from the retention in CamKII mice or their own wild-type littermates; suggesting that THK523 does not significantly bind to β-amyloid plaques and is selective for tau pathology *in vivo*.

Analysis of ^{18}F-THK523 biodistribution in the microPET studies showed no significant differences in ^{18}F-THK523 retention in the liver, intestine or bone between rTg4510 tau transgenic and wild-type mice. ^{18}F-THK523 retention in bone is indicative of some degree of defluorination (Van Dort *et al.*, 1995). *In vitro* stability testing showed that ^{18}F-THK523 was stable *in vitro*, suggesting that defluorination most likely occurs post-injection (data not shown). However, as the degree of free ^{18}F-bone retention is similar in both transgenic and control mice, the free ^{18}F does not

Downloaded from brain.oxfordjournals.org at Tohoku University on May 5, 2011

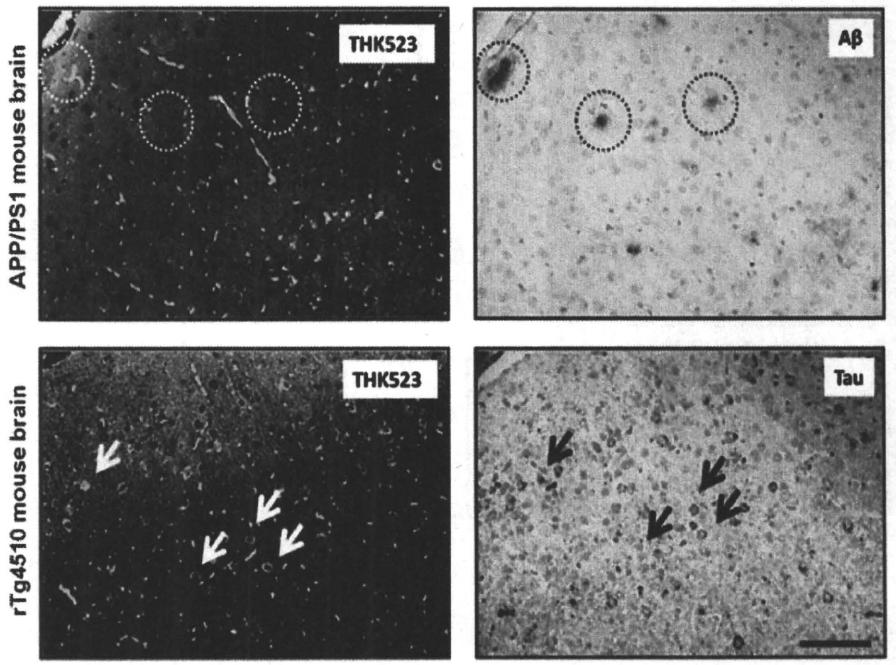

Figure 8 Co-localization of THK523 staining with tau pathology. Microscopy images of two serial sections (5 μm) from brains of rTg4510 and APP/PS1 mice immunostained with either tau (DAKO) or β-amyloid (1E8) antibodies, to identify tau tangles and β-amyloid (Aβ) plaques respectively; or stained with 10 nM THK523. Arrows indicate the location of tau tangles while circles indicate the location of β-amyloid plaques. Positive THK523 staining co-localize with tau immunostaining of neurofibrillary tangles, but not with β-amyloid plaques. Tissue sections were imaged with a Zeiss microscope and Axiocam digital camera. Scale bars: 100 μm. These data are representative of four independent studies employing eight rTg4510 and three APP/PS1 mice.

contribute differentially to the retention of ^{18}F-THK523 in the mouse brain. Similarly, as was observed in the *ex vivo* biodistribution studies, accumulation of radioactivity was observed within the intestine and liver of both rTg4510 and their control littermates indicating that most of the tracer and/or its metabolites were eliminated rapidly from the body through biliary excretion. Both tau transgenic and control littermates exhibited similar, low expression levels of tau in the liver (data not shown), further suggesting that ^{18}F-THK523 liver retention was due to the metabolic processing of ^{18}F-THK523 and not attributable to tau expression.

In conclusion, ^{18}F-THK523 is a novel tau radiotracer that fulfils the major criteria necessary for an 'ideal' PET radiotracer (Laruelle *et al.*, 2003; Nordberg, 2004). In addition to the abovementioned properties, THK523 was successfully labelled with ^{18}F with high specific activity. The relatively longer half-life of ^{18}F (110 min) precludes the need for an onsite cyclotron, allowing widespread distribution.

The clinical application of ^{18}F-THK523 as a selective tau imaging biomarker will provide important information regarding tau pathophysiology in Alzheimer's disease and non-Alzheimer's disease tauopathies, allowing correlation of brain tau load with cognitive function, monitoring disease progression and evaluation of therapeutic efficacy of newly developed drugs; especially aimed at modulating tau pathology (Gozes *et al.*, 2009; Hampel *et al.*, 2009*a*, *b*; Wischik and Staff, 2009). This study provides an important and critical step in defining the role of ^{18}F-THK523 as a tau specific PET radiotracer.

Acknowledgements

We thank Fairlie Hinton and Geoff Pavey from the Victorian Brain bank Network for sourcing and preparation of the human brain tissue.

Funding

National Health and Medical Research Council of Australia (in part); Neurosciences Victoria and the Ministry of Health, Labour and Welfare, Japan (in part); Industrial Technology Research Grant Program in 2009 from New Energy and Industrial Technology Development Organization (NEDO) of Japan(in part); AAR Viertel Fellowship (to M.T.F.-T.); NHMRC Senior Research Fellowship (to R.C. and K.J.B.). Perpetual Trustees H & L Hecht Trust.

References

Agdeppa ED, Kepe V, Liu J, Flores-Torres S, Satyamurthy N, Petric A, et al. Binding characteristics of radiofluorinated

Downloaded from brain.oxfordjournals.org at Tohoku University on May 5, 2011

6-dialkylamino-2-naphthylethylidene derivatives as positron emission tomography imaging probes for beta-amyloid plaques in Alzheimer's disease. J Neurosci 2001; 21: RC189.

Arriagada PV, Growdon JH, Hedley-Whyte ET, Hyman BT. Neurofibrillary tangles but not senile plaques parallel duration and severity of Alzheimer's disease. Neurology 1992; 42 (3 Pt 1): 631–9.

Barghorn S, Davies P, Mandelkow E. Tau paired helical filaments from Alzheimer's disease brain and assembled in vitro are based on beta-structure in the core domain. Biochemistry 2004; 43: 1694–703.

Blennow K, Hampel H. CSF markers for incipient Alzheimer's disease. Lancet Neurol 2003; 2: 605–13.

Cairns NJ, Ikonomovic MD, Benzinger T, Storandt M, Fagan AM, Shah A, et al. Absence of Pittsburgh compound B detection of cerebralamyloid beta in a patient with clinical, cognitive, and cerebrospinal fluidmarkers of Alzheimer disease. Arch Neurol 2009; 66: 1557–62.

Choi SR, Golding G, Zhuang Z, Zhang W, Lim N, Hefti F, et al. Preclinical properties of 18F-AV-45: a PET agent for Abeta plaques in the brain. J Nucl Med 2009; 50: 1887–94.

Delaere P, Duyckaerts C, Brion JP, Poulain V, Hauw JJ. Tau, paired helical filaments and amyloid in the neocortex: a morphometric study of 15 cases with graded intellectual status in aging and senile dementia of Alzheimer type. Acta neuropathologica 1989; 77: 645–53.

Delaere P, Duyckaerts C, Masters C, Beyreuther K, Piette F, Hauw JJ. Large amounts of neocortical beta A4 deposits without neuritic plaques nor tangles in a psychometrically assessed, non-demented person. Neurosci Lett 1990; 116: 87–93.

Dickson DW. Neuropathological diagnosis of Alzheimer's disease: a perspective from longitudinal clinicopathological studies. Neurobiology of aging 1997; 18 (Suppl 4): S21–6.

Dishino DD, Welch MJ, Kilbourn MR, Raichle ME. Relationship between lipophilicity and brain extraction of C-11-labeled radiopharmaceuticals. J Nucl Med 1983; 24: 1030–8.

Duyckaerts C, Brion JP, Hauw JJ, Flament-Durand J. Quantitative assessment of the density of neurofibrillary tangles and senile plaques in senile dementia of the Alzheimer type. Comparison of immunocytochemistry with a specific antibody and Bodian's protargol method. Acta neuropathologica 1987; 73: 167–70.

Duyckaerts C, Delaere P, Hauw JJ, Abbamondi-Pinto AL, Sorbi S, Allen I, et al. Rating of the lesions in senile dementia of the Alzheimer type: concordance between laboratories. A European multicenter study under the auspices of EURAGE. J Neurol Sci 1990; 97: 295–323.

Ferreira ST, Vieira MN, De Felice FG. Soluble protein oligomers as emerging toxins in Alzheimer's and other amyloid diseases. IUBMB Life 2007; 59: 332–45.

Fodero-Tavoletti MT, Rowe CC, McLean CA, Leone L, Li QX, Masters CL, et al. Characterization of PiB binding to white matter in Alzheimer disease and other dementias. J Nucl Med 2009; 50: 198–204.

Fodero-Tavoletti MT, Smith DP, McLean CA, Adlard PA, Barnham KJ, Foster LE, et al. In vitro characterization of Pittsburgh compound-B binding to Lewy bodies. J Neurosci 2007; 27: 10365–71.

Ganzer S, Arlt S, Schoder V, Buhmann C, Mandelkow EM, Finckh U, et al. CSF-tau, CSF-Abeta1-42, ApoE-genotype and clinical parameters in the diagnosis of Alzheimer's disease: combination of CSF-tau and MMSE yields highest sensitivity and specificity. J Neural Transm 2003; 110: 1149–60.

Gozes I, Stewart A, Morimoto B, Fox A, Sutherland K, Schmeche D. Addressing Alzheimer's disease tangles: from NAP to AL-108. Curr Alzheimer Res 2009; 6: 455–60.

Hampel H, Blennow K, Shaw LM, Hoessler YC, Zetterberg H, Trojanowski JQ. Total and phosphorylated tau protein as biological markers of Alzheimer's disease. Exp Gerontol 2009a; 45: 30–40.

Hampel H, Ewers M, Burger K, Annas P, Mortberg A, Bogstedt A, et al. Lithium trial in Alzheimer's disease: a randomized, single-blind, placebo-controlled, multicenter 10-week study. J Clin Psychiatry 2009b; 70: 922–31.

Ho GJ, Gregory EJ, Smirnova IV, Zoubine MN, Festoff BW. Cross-linking of beta-amyloid protein precursor catalyzed by tissue transglutaminase. FEBS Lett 1994; 349: 151–4.

Holcomb LA, Gordon MN, Jantzen P, Hsiao K, Duff K, Morgan D. Behavioral changes in transgenic mice expressing both amyloid precursor protein and presenilin-1 mutations: lack of association with amyloid deposits. Behav Genet 1999; 29: 177–85.

Ikonomovic MD, Klunk WE, Abrahamson EE, Mathis CA, Price JC, Tsopelas ND, et al. Post-mortem correlates of in vivo PiB-PET amyloid imaging in a typical case of Alzheimer's disease. Brain 2008; 131 (Pt 6): 1630–45.

Jack CR Jr, Knopman DS, Jagust WJ, Shaw LM, Aisen PS, Weiner MW, et al. Hypothetical model of dynamic biomarkers of the Alzheimer's pathological cascade. Lancet Neurol 2010; 9: 119–28.

Katzman R, Terry R, DeTeresa R, Brown T, Davies P, Fuld P, et al. Clinical, pathological, and neurochemical changes in dementia: a subgroup with preserved mental status and numerous neocortical plaques. Ann Neurol 1988; 23: 138–44.

Kepe V, Huang SC, Small GW, Satyamurthy N, Barrio JR. Visualizing pathology deposits in the living brain of patients with Alzheimer's disease. Methods Enzymol 2006; 412: 144–60.

Klunk WE, Engler H, Nordberg A, Wang Y, Blomqvist G, Holt DP, et al. Imaging brain amyloid in Alzheimer's disease with Pittsburgh Compound-B. Ann Neurol 2004; 55: 306–19.

Klunk WE, Lopresti BJ, Ikonomovic MD, Lefterov IM, Koldamova RP, Abrahamson EE, et al. Binding of the positron emission tomography tracer Pittsburgh compound-B reflects the amount of amyloid-beta in Alzheimer's disease brain but not in transgenic mouse brain. J Neurosci 2005; 25: 10598–606.

Lambert MP, Viola KL, Chromy BA, Chang L, Morgan TE, Yu J, et al. Vaccination with soluble Abeta oligomers generates toxicity-neutralizing antibodies. J Neurochem 2001; 79: 595–605.

Laruelle M, Slifstein M, Huang Y. Relationships between radiotracer properties and image quality in molecular imaging of the brain with positron emission tomography. Mol Imaging Biol 2003; 5: 363–75.

Lee VM, Goedert M, Trojanowski JQ. Neurodegenerative tauopathies. Annu Rev Neurosci 2001; 24: 1121–59.

LeVine H 3rd. Quantification of beta-sheet amyloid fibril structures with thioflavin T. Methods Enzymol 1999; 309: 274–84.

Maeda J, Ji B, Irie T, Tomiyama T, Maruyama M, Okauchi T, et al. Longitudinal, quantitative assessment of amyloid, neuroinflammation, and anti-amyloid treatment in a living mouse model of Alzheimer's disease enabled by positron emission tomography. J Neurosci 2007; 27: 10957–68.

Maezawa I, Hong HS, Liu R, Wu CY, Cheng RH, Kung MP, et al. Congo red and thioflavin-T analogs detect Abeta oligomers. J Neurochem 2008; 104: 457–68.

McLean CA, Cherny RA, Fraser FW, Fuller SJ, Smith MJ, Beyreuther K, et al. Soluble pool of Abeta amyloid as a determinant of severity of neurodegeneration in Alzheimer's disease. Annals Neurol 1999; 46: 860–6.

Ng S, Villemagne VL, Berlangieri S, Lee ST, Cherk M, Gong SJ, et al. Visual assessment versus quantitative assessment of 11C-PIB PET and 18F-FDG PET for detection of Alzheimer's disease. J Nucl Med 2007; 48: 547–52.

Nordberg A. PET imaging of amyloid in Alzheimer's disease. Lancet Neurol 2004; 3: 519–27.

Okamura N, Suemoto T, Furumoto S, Suzuki M, Shimadzu H, Akatsu H, et al. Quinoline and benzimidazole derivatives: candidate probes for in vivo imaging of tau pathology in Alzheimer's disease. J Neurosci 2005; 25: 10857–62.

Perez M, Valpuesta JM, Medina M, Montejo de Garcini E, Avila J. Polymerization of tau into filaments in the presence of heparin: the minimal sequence required for tau-tau interaction. J Neurochem 1996; 67: 1183–90.

Pike VW. PET radiotracers: crossing the blood-brain barrier and surviving metabolism. Trends Pharmacol Sci 2009; 30: 431–40.

Downloaded from brain.oxfordjournals.org at Tohoku University on May 5, 2011

Pike KE, Savage G, Villemagne VL, Ng S, Moss SA, Maruff P, et al. Beta-amyloid imaging and memory in non-demented individuals: evidence for preclinical Alzheimer's disease. Brain 2007; 130 (Pt 11): 2837–44.

Rowe CC, Ackerman U, Browne W, Mulligan R, Pike KL, O'Keefe G, et al. Imaging of amyloid beta in Alzheimer's disease with 18F-BAY94-9172, a novel PET tracer: proof of mechanism. Lancet Neurol 2008; 7: 129–35.

Rowe CC, Ng S, Ackermann U, Gong SJ, Pike K, Savage G, et al. Imaging beta-amyloid burden in aging and dementia. Neurology 2007; 68: 1718–25.

Shoghi-Jadid K, Small GW, Agdeppa ED, Kepe V, Ercoli LM, Siddarth P, et al. Localization of neurofibrillary tangles and beta-amyloid plaques in the brains of living patients with Alzheimer disease. Am J Geriatr Psychiatry 2002; 10: 24–35.

van der Zee J, Sleegers K, Van Broeckhoven C. Invited article: the Alzheimer disease-frontotemporal lobar degeneration spectrum. Neurology 2008; 71: 1191–7.

Van Dort ME, Jung YW, Sherman PS, Kilbourn MR, Wieland DM. Fluorine for hydroxy substitution in biogenic amines: asymmetric synthesis and biological evaluation of fluorine-18-labeled beta-fluorophenylalkylamines as model systems. J Med Chem 1995; 38: 810–5.

von Bergen M, Barghorn S, Jeganathan S, Mandelkow EM, Mandelkow E. Spectroscopic approaches to the conformation of tau protein in solution and in paired helical filaments. Neurodegener Dis 2006; 3: 197–206.

Walsh DM, Klyubin I, Fadeeva JV, Cullen WK, Anwyl R, Wolfe MS, et al. Naturally secreted oligomers of amyloid beta protein potently inhibit hippocampal long-term potentiation in vivo. Nature 2002; 416: 535–9.

Wenk GL. Neuropathologic changes in Alzheimer's disease. J Clin Psychiatry 2003; 64 (Suppl 9): 7–10.

Wischik C, Staff R. Challenges in the conduct of disease-modifying trials in Alzheimer's disease: practical experience from a phase 2 trial of Tau-aggregation inhibitor therapy. J Nutr Health Aging 2009; 13: 367–9.

Wisniewski HM, Bancher C, Barcikowska M, Wen GY, Currie J. Spectrum of morphological appearance of amyloid deposits in Alzheimer's disease. Acta Neuropathol 1989; 78: 337–47.

Downloaded from brain.oxfordjournals.org at Tohoku University on May 5, 2011

doi:10.1093/brain/awq091 Brain 2010: 133; 1772–1778 | 1772

BRAIN
A JOURNAL OF NEUROLOGY

In vivo visualization of α-synuclein deposition by carbon-11-labelled 2-[2-(2-dimethylaminothiazol-5-yl)ethenyl]-6-[2-(fluoro)ethoxy]benzoxazole positron emission tomography in multiple system atrophy

Akio Kikuchi,[1] Atsushi Takeda,[1] Nobuyuki Okamura,[2] Manabu Tashiro,[3] Takafumi Hasegawa,[1] Shozo Furumoto,[2,4] Michiko Kobayashi,[1] Naoto Sugeno,[1] Toru Baba,[1] Yasuo Miki,[5] Fumiaki Mori,[5] Koichi Wakabayashi,[5] Yoshihito Funaki,[4] Ren Iwata,[4] Shoki Takahashi,[6] Hiroshi Fukuda,[7] Hiroyuki Arai,[8] Yukitsuka Kudo,[9] Kazuhiko Yanai[2] and Yasuto Itoyama[1]

1 Department of Neurology, Graduate School of Medicine, Tohoku University, Sendai, 980-8574 Japan
2 Department of Pharmacology, Graduate School of Medicine, Tohoku University, Sendai, 980-8575 Japan
3 Division of Cyclotron Nuclear Medicine, Cyclotron and Radioisotope Centre, Tohoku University, Sendai, 980-8578 Japan
4 Division of Radiopharmaceutical Chemistry, Cyclotron and Radioisotope Centre, Tohoku University, Sendai, 980-8578 Japan
5 Department of Neuropathology, Institute of Brain Science, Hirosaki University Graduate School of Medicine, Hirosaki, 036-8562 Japan
6 Department of Diagnostic Radiology, Graduate School of Medicine, Tohoku University, Sendai, 980-8575 Japan
7 Department of Nuclear Medicine and Radiology, Institute of Development, Ageing and Cancer, Tohoku University, Sendai, 980-8575 Japan
8 Department of Geriatric and Respiratory Medicine, Institute of Development, Ageing and Cancer, Tohoku University, Sendai, 980-8575 Japan
9 Innovation of New Biomedical Engineering Centre, Tohoku University, Sendai, 980-8574 Japan

Correspondence to: Atsushi Takeda,
Department of Neurology,
Graduate School of Medicine,
Tohoku University,
1-1 Seiryo-machi,
Aoba-ku, Sendai, Miyagi,
980-8574, Japan
E-mail: atakeda@em.neurol.med.tohoku.ac.jp

The histopathological hallmark of multiple system atrophy is the appearance of intracellular inclusion bodies, named glial cytoplasmic inclusions, which are mainly composed of α-synuclein fibrils. *In vivo* visualization of α-synuclein deposition should be used for the diagnosis and assessment of therapy and severity of pathological progression in multiple system atrophy. Because 2-[2-(2-dimethylaminothiazol-5-yl)ethenyl]-6-[2-(fluoro)ethoxy] benzoxazole could stain α-synuclein-containing glial cytoplasmic inclusions in post-mortem brains, we compared the carbon-11-labelled 2-[2-(2-dimethylaminothiazol-5-yl)ethenyl]-6-[2-(fluoro)ethoxy] benzoxazole positron emission tomography findings of eight multiple system atrophy cases to those of age-matched normal controls. The positron emission tomography data demonstrated high distribution volumes in the subcortical white matter (uncorrected $P<0.001$), putamen and posterior cingulate cortex (uncorrected $P<0.005$), globus pallidus, primary motor cortex and anterior cingulate cortex (uncorrected $P<0.01$), and substantia nigra (uncorrected $P<0.05$) in multiple system atrophy cases compared to the normal controls. They were coincident with glial cytoplasmic inclusion-rich brain areas in

Received January 13, 2010. Revised March 15, 2010. Accepted March 17, 2010. Advance Access publication April 29, 2010
© The Author (2010). Published by Oxford University Press on behalf of the Guarantors of Brain. All rights reserved.
For Permissions, please email: journals.permissions@oxfordjournals.org

Downloaded from brain.oxfordjournals.org at Tohoku University on May 8, 2011

multiple system atrophy and thus, carbon-11-labelled 2-[2-(2-dimethylaminothiazol-5-yl)ethenyl]-6-[2-(fluoro)ethoxy] benzoxazole positron emission tomography is a promising surrogate marker for monitoring intracellular α-synuclein deposition in living brains.

Keywords: glial cytoplasmic inclusion; Lewy body; β-amyloid; Parkinson's disease; Pittsburgh compound B

Abbreviations: BF-227 = 2-[2-(2-dimethylaminothiazol-5-yl)ethenyl]-6-[2-(fluoro)ethoxy]benzoxazole; MSA = multiple system atrophy; PIB = Pittsburgh compound B

Introduction

Multiple system atrophy (MSA) is a sporadic, progressive neurodegenerative disease characterized by variable severity of parkinsonism, cerebellar ataxia, autonomic failure and pyramidal signs. Although MSA was originally described as three separate diseases [olivopontocerebellar atrophy (Dejerine and Thomas, 1900), striatonigral degeneration (van der Eecken *et al.*, 1960) and Shy–Drager syndrome (Shy and Drager, 1960)], they are currently classified into a single disease that consists of MSA with predominant parkinsonism and MSA with predominant cerebellar ataxia (Gilman *et al.*, 1999). The histopathological hallmark of MSA, glial cytoplasmic inclusions, comprises mainly insoluble fibrils of phosphorylated α-synuclein (Wakabayashi *et al.*, 1998). Thus, it is suggested that the MSA is in the family of α-synucleinopathies (Marti *et al.*, 2003) including Parkinson's disease and dementia with Lewy bodies, which are characterized by the presence of Lewy bodies, representing other brain inclusions composed of α-synuclein.

Previous neuropathological studies indicated that the appearance of glial cytoplasmic inclusions preceded the clinical onset of MSA (Fujishiro *et al.*, 2008) and the amount of α-synuclein deposition correlated with the disease progression (Wakabayashi and Takahashi, 2006). Therefore, it is plausible that the formation of α-synuclein deposits plays a key role in neurodegeneration, and that compounds that inhibit this process may be therapeutically useful for MSA and other α-synucleinopathies. In fact some compounds, including antioxidants (Ono and Yamada, 2006) and non-steroidal anti-inflammatory drugs (Hirohata *et al.*, 2008), were reported to have potent anti-fibrillogenic and fibril-destabilizing effects on aggregated α-synucleins, and received much attention as possible new therapeutic agents (Ono and Yamada, 2006; Hirohata *et al.*, 2008). Detection of α-synuclein deposition *in vivo* could theoretically allow early diagnosis even at the presymptomatic stage, as well as assess disease progression and possible therapeutic effects in the living brain of patients with MSA.

Although Pittsburgh compound B (PIB) and other compounds were reported to be useful in detecting senile plaques *in vivo*, to our knowledge, there were no imaging probes currently available for *in vivo* detection of α-synuclein deposition. Recently, 2-[2-(2-dimethylaminothiazol-5-yl)ethenyl]-6-[2-(fluoro)ethoxy] benzoxazole (BF-227), known as a positron emission tomography (PET) probe for *in vivo* detection of dense β-amyloid deposits in humans (Kudo *et al.*, 2007), was reported to bind with synthetic α-synuclein aggregates as well as β-amyloid fibrils *in vitro* (Fodero-Tavoletti *et al.*, 2009). In the present study, we demonstrated that BF-227 could stain α-synuclein-containing glial cytoplasmic inclusions in post-mortem tissues and moreover, that a PET study with carbon-11-labelled BF-227 ([11C]-BF-227) could detect α-synuclein deposits in the living brains of patients with MSA.

Materials and methods

Neuropathological staining

Brain specimens

The subjects of the first part of the study were nine autopsy cases, including three with Parkinson's disease, three with dementia with Lewy bodies and three with MSA. The above diagnoses were confirmed both clinically and histopathologically. Brain tissues taken from the temporal cortex and substantia nigra of patients with Parkinson's disease and dementia with Lewy bodies, and pontine base of patients with MSA, were fixed in 20% buffered formalin for 72 h at 4°C, and vibratome sections (50 μm thick) were prepared.

Fluorescence and immunohistochemical analysis

BF-227 was dissolved in 50% ethanol containing 5% polysorbate (Tween 80; Wako, Osaka, Japan). The sections were slide mounted, incubated in 100 μM BF-227 for 30 min, dipped three times in phosphate buffer, and coverslipped with non-fluorescent mounting medium (Vectashield, Vector Laboratories, Burlingame, CA, USA). Fluorescence images were visualized using an Olympus Provis fluorescence microscope (Olympus, Tokyo, Japan) at wavelength 400 nm. After photographing fluorescent structures, BF-227-labelled sections were immunostained with primary antibodies against phosphorylated α-synuclein (#64; Wako). For phosphorylated α-synuclein immunohistochemistry, the sections were pre-treated with 99% formic acid for 5 min, then incubated overnight at 4°C with each primary antibody followed by incubation with the biotinylated secondary antibodies and the avidin–biotin–peroxidase complex (Vectastain ABC kit, Vector Laboratories). Diaminobenzidine was used as the chromogen.

PET study

Subjects

Eight patients with probable MSA and eight age-matched normal subjects were studied to examine the distribution of [11C]-BF-227 in the brain. All probable MSA patients were diagnosed on the second consensus criteria for probable MSA (Gilman *et al.*, 2008). Table 1 summarizes the clinical features of these patients. There were no significant differences in age, disease duration and unified MSA rating scale score between the MSA with predominant parkinsonism

Downloaded from brain.oxfordjournals.org at Tohoku University on May 9, 2011

Table 1 Subject profile

	Normal controls	MSA		
		Total	MSA-P	MSA-C
n	8	8	4	4
Gender (F/M)	4/4	4/4	1/3	3/1
Age (years)	64.3 ± 5.90	57.4 ± 10.1	60.5 ± 11.1	54.3 ± 9.50
Duration (years)		1.50 ± 0.54	1.75 ± 0.50	1.25 ± 0.50
UMSARS score		36.1 ± 8.87	41.5 ± 9.39	30.8 ± 4.27

Data are mean ± SD.
MSA-P = MSA with predominant parkinsonism; MSA-C = MSA with predominant cerebellar ataxia; UMSARS = unified MSA rating scale.

subgroup and the MSA with predominant cerebellar ataxia subgroup. The normal control group comprised volunteers without impairment of cognitive and motor functions who had no cerebrovascular lesions on magnetic resonance imaging. The study protocol was approved by the Ethical Committee of Tohoku University Graduate School of Medicine, and a written informed consent was obtained from each subject after being given a complete description of the study.

Radiosynthesis of [^{11}C]-BF-227

BF-227 and its N-desmethylated derivative (a precursor of [^{11}C]-BF-227) were custom-synthesized by Tanabe R&D Service Co. (Tokyo) (Kudo *et al.*, 2007). [^{11}C]-BF-227 was synthesized from the precursor by N-methylation in dimethyl sulphoxide using [^{11}C]-methyl triflate (Jewett, 1992; Iwata *et al.*, 2001). After quenching the reaction with 5% acetic acid in ethanol, [^{11}C]-BF-227 was separated from the crude mixture by semi-preparative reversed-phase high-performance liquid chromatography and then isolated from the collected fraction by solid-phase extraction. The purified [^{11}C]-BF-227 was solubilized in isotonic saline containing 1% polysobate-80 and 5% ascorbic acid. The saline solution was filter sterilized with a 0.22 mm Millipore® filter for clinical use. The radiochemical yields were >50% based on [^{11}C]-methyl triflate, and the specific radioactivities were 119–138 GBq/mmol at the end of synthesis. The radiochemical purities were >95%.

PET procedure

The [^{11}C]-BF-227 PET study was performed using a SET-2400W PET scanner (Shimadzu Inc., Japan) under resting condition with eyes closed in a dark room. Following a 68Ge/Ga transmission scan of 300–400 s duration, an emission scan was started soon after intravenous injection of 3.7–8.3 mCi of [^{11}C]-BF-227. A dynamic series of PET scans were acquired over 60 min with 23 frames. Emission data were corrected for attenuation, dead time and radioactive decay. Standardized uptake value images were obtained by normalizing tissue concentration by the injected dose and body mass. Arterial blood samples (1.5 ml) from the radial or brachial artery were collected from each subject at 10 s intervals for the first 2 min, and subsequently at intervals increasing progressively from 1 to 10 min until 60 min after the injection of [^{11}C]-BF-227 except for one subject, from whom arterialized venous blood samples (1.5 ml) from a hand vein heated in a far-infrared mat were collected at the same time intervals. The plasma obtained by centrifugation at 3000*g* for 3 min was weighed and the radioactivity was measured with a well-type scintillation counter. Additional arterial blood samples were obtained at four time points during the study (5, 15, 30 and 60 min) for the determination of radiolabelled metabolites in plasma using high-performance liquid chromatography. These data yielded values of the unchanged fraction of parent radiotracer throughout the time frame of the study. A multi-exponential equation was used to describe this curve and to estimate the parent fraction at each measured plasma curve time point.

PET image analysis

To measure α-synuclein deposition densities in the brain, the distribution volume, the ratio of [^{11}C]-BF-227 concentration in tissue to that in plasma at equilibrium, was calculated by Logan's graphical analysis (Logan, 2000), since BF-227 reversibly binds to α-synuclein depositions (Tashiro *et al.*, 2009). Region of interest analysis was performed to evaluate the regional distribution of [^{11}C]-BF-227. Circular regions of interest were placed on individual axial PET images in the frontal cortex, primary motor cortex, parietal cortex, medial temporal cortex, lateral temporal cortex, occipital cortex, anterior cingulate cortex, posterior cingulate cortex, subcortical white matter, caudate nucleus, putamen, globus pallidus, thalamus, substantia nigra, midbrain tegmentum, pons and cerebellar cortex, referring to the individual magnetic resonance images.

Statistical analysis

Data were expressed as mean ± SD. Differences in distribution volume between normal control and MSA groups were evaluated by one-way analysis of variance followed by Bonferroni's multiple comparison test (GraphPad Prism Software).

Results

Neuropathological staining

In the post-mortem brains with Parkinson's disease, double-labelling immunostaining with BF-227 fluorostaining and anti-phosphorylated α-synuclein antibody demonstrated co-localization of the proteins in Lewy bodies in the substantia nigra (Fig. 1A and B). Strong BF-227 staining was observed in the central core (Fig. 1A). BF-227 was also detected in the cortical Lewy bodies in dementia with Lewy bodies (Fig. 1C and D). In MSA, double-labelling experiments using BF-227 and anti-phosphorylated α-synuclein antibody demonstrated BF-227 fluorescent signal in the most of glial cytoplasmic inclusions in the pontine base (Fig. 1E and F).

PET study

Tissue time activity curves of [^{11}C]-BF-227 in the brain indicated more gradual clearance from the brain in patients with MSA compared with normal subjects following initial rapid uptake of radioactivity (Fig. 2A). Relatively high concentrations of [^{11}C]-BF-227 radioactivity were observed in the subcortical white matter and lenticular nucleus in MSA, in which relatively intense α-synuclein deposits were found in the post-mortem brain (Fig. 2B). [^{11}C]-BF-227 exhibited linear regression curves on Logan plot analysis in all brain regions examined. Since the slopes of the regression lines represent the distribution volume of the tracer, these findings indicated a higher distribution volume of [^{11}C]-BF-227 in MSA than in normal controls (Fig. 2C). The regional distribution volume values were high in the subcortical white matter (uncorrected $P < 0.001$), putamen and posterior cingulate cortex

Downloaded from brain.oxfordjournals.org at Tohoku University on May 8, 2011